SAND77-0913
Unlimited Release
UC-21

The Application of Inertial Confinement Fusion to Weapon Technology

Alan J. Toepfer, Laurence D. Posey

Prepared by Sandia Laboratories, Albuquerque, New Mexico 87185 and Livermore, California 94550 for the United States Department of Energy under Contract AT(29–1)-789

Printed December 1978

Sandia Laboratories

SF 2900 Q(7-73)

DISCLAIMER

Issued by Sandia Laboratories, operated for the United States Department of Energy by Sandia Corporation.

PAGES 1 to 2

WERE INTENTIONALLY

LEFT BLANK

SAND77-0913
Unlimited Release
Printed December 1978

Distribution
Category UC-21

THE APPLICATION OF INERTIAL CONFINEMENT FUSION TO WEAPON TECHNOLOGY

Alan J. Toepfer
Electron Beam Research Division 4242

Laurence D. Posey
Beam Source Application Division 4452

Sandia Laboratories
Albuquerque, NM 87185

ABSTRACT

This report reviews aspects of the military applications of the inertial confinement fusion (ICF) program at Sandia Laboratories. These applications exist in the areas of: (1) weapon physics research, and (2) weapon effects simulation. In the area of weapon physics research, ICF source technology can be used to study: (1) equations-of-state at high energy densities, (2) implosion dyanmics, and (3) laboratory simulation of exoatmospheric burst phenomena. In the area of weapon effects simulation, ICF technology and facilities have direct near, intermediate, and far term applications. In the near term, short pulse x-ray simulation capabilities exist for electronic component effects testing. In the intermediate term, capabilities can be developed for high energy neutron exposures and bremsstrahlung x-ray exposures of components. In the far term, system level exposures of full reentry vehicles will be possible if sufficiently high pellet gains are achieved.

CONTENTS

THE APPLICATION OF INERTIAL CONFINEMENT FUSION TO WEAPON TECHNOLOGY

I. Introduction and Summary

The demonstration of inertial confinement fusion using lasers and intense charged particle beams is the result of work which grew out of the national nuclear weapons research and development program. The development of nonnuclear high power sources of energy has resulted in the hope of harnessing inertial confinement fusion on a scale which can lead to peaceful power production. At the same time, the technology that grew out of the weapon program still has application to those programs as to the development of new weapon concepts.

The particle and laser beam fusion programs (Figure 1) at Sandia Laboratories germinated from a pulsed power technology which was developed to simulate nuclear weapons effects. This capability has grown into a comprehensive effort including both target physics research and particle beam and laser technology development, which have military applications in the areas of weapons physics research and weapons effects simulation.

In pursuing the goal of inertial confinement fusion, Sandia interacts with the other ERDA laboratories and DNA contractors. The major nuclear design laboratories provide Sandia with expertise in the area of target design and fabrication, and Sandia provides a pulse-power technology base for LLL and LASL programs. For ICF, Sandia has concentrated on the development of short-pulse (< 50 nsec) accelerator technology. The laboratories carrying out work relevant to the weapons effects simulation requirements of the Defense Nuclear Agency have concentrated on the development of long pulse accelerator technology. This work has led to the development of sources of interest to inertial confinement fusion by the DNA contractors, and pulse-power technology development of interest to DNA by Sandia.

This report is a review of the military applications of the inertial confinement fusion program. Within the areas discussed above, specific applications and the relevance of inertial confinement research to meeting the source requirements, broadening the data base, and developing the new technology for the fulfillment of these applications are discussed. In particular, the applications realized at the present time, applications which are projected to be realized from the present time to the achievement of high energy gain from pellets, and applications projected to be realized after achievement of high energy gain are reviewed. Finally, the contribution of ICF research and capabilities is quantified by comparison with alternative technologies.

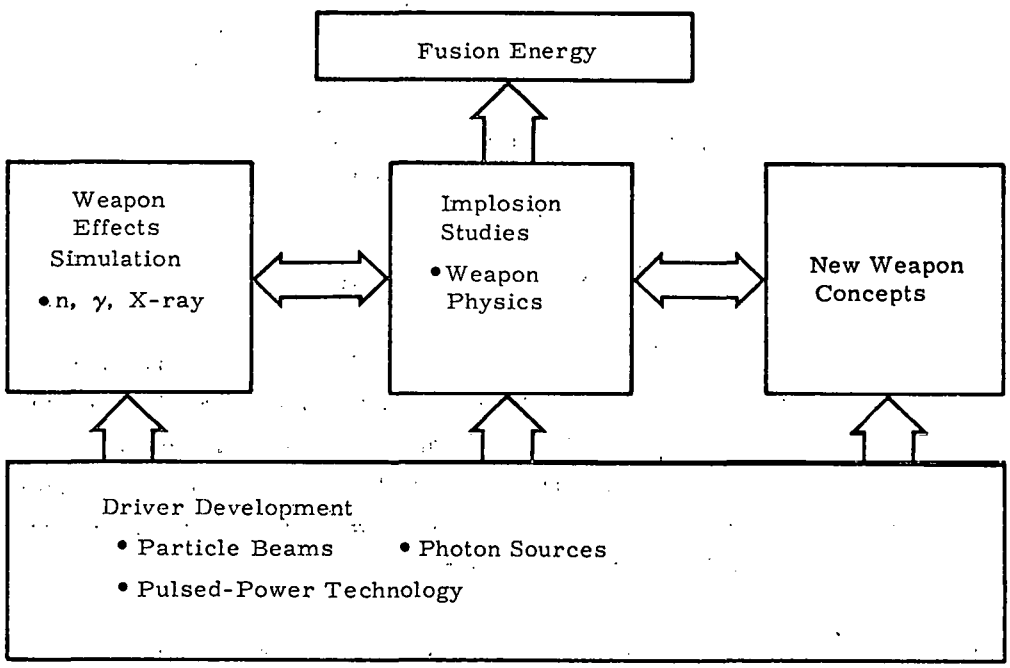

Figure 1. Sandia Inertial Confinement Fusion

This report contains two sections outlining the applications. Section II is a review of the areas of weapon physics research which can be studied using inertial confinement fusion source technology. Because of high shot rate and low cost per shot, ICF sources at present and in the intermediate and far terms provide a useful technology for conducting weapon physics experiments. A summary of past accomplishments is given in Appendix A. Section III deals with utilization of ICF sources for weapons effects simulation. The capabilities of ICF sources and technology for x-ray, gamma ray, and neutron production are reviewed. Present and intermediate term source technology makes possible the simulation of gamma ray effects using realistic pulse widths and exposures. For testing of complete weapons systems in a synergistic environment, far term ICF high gain pellet experiments are a possible alternative to underground testing for satisfying simulation requirements.

II. Application of Inertial Confinement Fusion to Weapon Physics

ICF Source Capabilities

Charged particle and laser beams are capable of concentrating large amounts of energy at high power flux levels onto small targets. The resulting temperatures and pressures attained in the targets are orders of magnitude larger than can be achieved in the laboratory environment by mechanical means and surpass those obtainable with chemical explosives. At present, intense relativistic electron beams have delivered 10^{12} W/cm^2 and deposited energies approaching 10^{12} to 10^{13} ergs per gram in millimeter size targets. With existing relativistic electron beam

accelerators such as Hydra (0.5 TW, 60 nsec) and Proto I (1.5 TW, 24 nsec), shock strengths in the 1 to 10 megabar regime can be achieved. With intermediate term facilities such as EBFA-I shock strengths in the 10 to 100 megabar regime are projected.

These parameters span a crucial range of pressures for which little data are available on hydrodynamic behavior and material equations of state. The complexity of inertial confinement fusion target experiments requires that they be analyzed by simulating the experiment with one- and two-dimensional hydrocodes. Thus, verification and improvement of weapon design codes will be an intrinsic part of the inertial confinement fusion experiments. In addition, a variety of new ideas have been and will continue to be developed in the course of designing inertial confinement fusion targets. Many of these concepts appear to be applicable to weapon design. Also, the dynamics and stability of implosions can be studied using particle beam drivers.

The irradiation of solid spherical pellets with high intensity lasers can produce nearly spherical plasma expansions which can be used to simulate some aspects of high altitude nuclear explosions. Characterization of the atmospheric state produced by a single burst is necessary for several reasons: (1) prediction of the effects of subsequent bursts in a multiburst environment; (2) evaluation of the spatial extent and duration of satellite communications interference, and (3) evaluation of radar shielding effects which hinder detection of secondary missions.

Alternatives

Various alternatives to inertial confinement fusion sources are available and have been used to study certain aspects of weapons physics. The two-stage gas gun facility at Sandia has been applied to material response studies which have direct application to the Lawrence Livermore Laboratory and Los Alamos Scientific Laboratory weapons programs. Successful experimental and diagnostic techniques developed on the gas gun facility have been extended to higher energy density levels using Sandia's ICF electron beam accelerators.

Explosively driven systems have been traditionally used to study equation-of-state and implosion physics at high energies. One-dimensional flyer plate experiments can be carried out relatively inexpensively. Implosion experiments require a substantially larger investment in a flash radiography diagnostic, such as Phermex at Los Alamos. Latest designs of such flash x-ray accelerators such as the Physics International Pulserad 1480 used by the French AEC employ inertial confinement fusion related accelerator technology.

High altitude barium releases have been an experimental technique utilized to study problems related to interaction of nuclear burst debris with the upper atmosphere.

For testing of weapons concepts, underground nuclear explosions have been traditionally utilized by the weapons laboratories. This is the only source for attaining energy density levels needed to expand the data base into the range of parameters required for weapon design. These tests are extremely expensive, 20 to 30 million dollars per shot for a weapon effects test, or

3 to 5 million dollars for a dedicated shot to test a given weapon design. The shot rate is extremely low compared to that which can be attained from inertial confinement fusion experiments.

Because of their low initial cost and high shot rate, particle beam inertial confinement fusion sources, to the extent that they can study certain aspects of weapon physics, are cost effective. Table I lists the shot rate per year and estimated cost to the user per shot for experiments on various ICF sources. These estimates are based on experience with existing sources and affect the cost of operation of the source as a user facility (capital investment and operating budget) and do not include the cost of the experiment itself, which can vary appreciably according to the type of experiment fielded.

Even ignoring the probability of a comprehensive test ban treaty, present and planned inertial confinement fusion sources are an attractive resource for continuing a weapon physics research program.

o

III. Application of Inertial Confinement Fusion to Weapon Effects Simulation

Requirements and Capabilities

In order to assess the hardness of weapons systems and their components to threat radiation environments, a variety of simulation capabilities has been developed. These include laboratory capabilities for above ground testing where in general the components of the threat environment are dealt with separately, and underground testing capabilities for which all the radiation components are present. In the latter case, synergistic effects can be studied. In light of this synergistic capability, underground test exposures are often viewed as proof tests of systems and components. These capabilities have been developed by both the DOD and ERDA to satisfy requirements in their respective areas of responsibility. In many cases, the effects produced by threat environments are simulated but the environment itself is not. This is especially true for above-ground capabilities. But even the components of the underground test environment are found to be deficient in some aspects. As compared to the system threats, examples of this are the short pulse widths for x-rays and gamma rays, the shortened time interval between the x-ray and gamma-ray arrival and that of the neutrons, and the relative intensities of the radiation components. This results from the fact that the yields of the devices used for underground testing are generally much less than those corresponding to the system threats.

The total radiation environment can be quite complex but is generally composed of x-ray, gamma ray, neutron, and EMP components. The intensity of the various components is strongly dependent upon the specific system in place of the mission under consideration.

TABLE I

ICF Source Capabilities for Equation-of-State (EOS), Implosion (IMP), and Exatmospheric Nuclear Burst (NB) Experiments

Source	Cap. Inv. (M$)* Source	Bldg.	Operating* M$/Yr	Shot/Yr.	Cost/Shot* K$	Experiments EOS	IMP	NB
I. Particle Beam (ICF)								
Hydra	.60	.10	.25	700	.5	✓	✓	X
Proto I	1.4	.15	.25	300	1.3	✓	✓	X
Proto II	1.5	.27	.5 †	300†	2.2†	1Q/78	1Q/78	X
EBFA I	9.2	5.0	1.0 †	150†	15.0†	1Q/81	1Q/81	?
EBFA II	10.0†	5.0 †	1.5 †	100†	28.0†	4Q/84	4Q/84	?
II. Laser (ICF)								
Argus (LLL)	3.5	--	--	--	--	?	✓	✓
Shiva (LLL)	26.2	8.8	--	--	--	?	3Q/77	3Q/77
Shiva-Nova (LLL)	185.0	--	--	--	--	?	1Q/83	1Q/83
Two-Beam(LASL)	1.0	.4	--	2000	--	?	✓	✓
HEGLF (LASL)	45.0	9.5	4.0 †	200†	45 †	?	1Q/82	1Q/82
200 kJ HF (SLA)‡	25.0†	5.0†	1.6 †	100†	44 †	?	1Q/82	1Q/82

* - FY76 Dollars

† - Estimated

‡ Preliminary estimate for this document.

✓ - Experiment has been done or possible on indicated date (Quarter/FY).

? - Experiment proposed.

X - Experiment not possible or extremely difficult.

Testing requirements can generally be broken down into a number of categories. These correspond to the testing of the various parts of a weapons system separately prior to the testing of assembled units. Of course, the largest exposure requirement (primarily DOD responsibility) is that for the full system; RV, missile, satellite, etc.

The culmination of weapons effects testing in support of weapons system development programs is the final "proof" test of the system. As mentioned earlier, this is presently carried out using underground testing. Since underground testing is but a simulation capability itself, there are limitations associated with its use. In the event that a comprehensive test-ban treaty were to become a reality, this synergistic testing capability would no longer be available to the weapons effects community. In light of these considerations, it appears that inertial confinement fusion is a possible alternative to underground testing in order to satisfy weapons effects testing requirements. Although inertial confinement fusion will have many of the same shortcomings as underground testing it appears to be an approach to satisfy both the x-ray component and the synergistic requirements in the foreseeable future.

Inertial Confinement Fusion Capabilities

The development program as laid out by the Division of Laser Fusion includes a number of facilities which are stepping stones to the final goal of energy gain from pellet burn. These various facilities will have rather limited inertial confinement fusion capabilities but may be used in other modes of operation to satisfy many weapon effects requirements.

Weapon effects simulation utilization of existing machines such as Proto I and Proto II or intermediate term machines such as EBFA I will provide a useful x-ray simulation capability when operated in the bremsstrahlung mode. Also, these high current machines could be of value for driving high energy gas lasers which may then be used to produce an x-ray environment for testing purposes. Far term accelerators such as EBFA II should provide a capability for providing useful simulation environment in the pellet burn mode. The use of EBFA II or other high power inertial confinement fusion facilities operating in the pellet burn mode will allow synergistic exposure of weapon system components and units.

Since the possibility exists that a comprehensive test ban treaty could be negotiated, inertial confinement sources may be the only possibilities available in the future for synergistic weapons effects testing. For weapons effects simulation, a single shot system would suffice. Therefore, the requirements for inertial confinement fusion sources will probably be less severe for weapons testing applications than for civilian power applications. In any case, if inertial confinement reactions are achieved, simulation should be less costly than underground testing. Averaging the costs of the last 5 Nevada Test Site (NTS) events indicates that for tests conducted in a tunnel the average cost is of the order of 20 million dollars, exclusive of the Laboratories' labor. A typical vertical line-of-sight effects test cost 1/3 as much, incorporates about the same area, but has about 1/3 the data channels. In contrast, it is anticipated that the entire EBFA II facility will cost

approximately 30 million dollars. It could, of course, be used repeatedly. Future facilities capable of higher pellet gains should be available at a cost of between 100 and 200 million dollars. It appears that ICF sources could be attractive for full system testing in the future.

IV. Conclusions

The Sandia inertial confinement fusion program has military applications to the development of advanced weapon concepts and nuclear weapon effects simulation

Inertial confinement fusion drivers can be used as a tool to study the physics of interest to nuclear weapon design and exoatmospheric burst phenomena in the laboratory. Some work is already being carried out on existing facilities. Intermediate and far-term drivers will be capable of studying parameter regimes of high-energy density which approach or attain levels produced in underground nuclear tests. If a comprehensive test ban treaty is negotiated, inertial confinement fusion sources will be an important experimental tool for weapon designers. The type of information to be gained in inertial confinement fusion experiments will provide a data base for improved weapon design and effects evaluation.

Utilization of inertial confinement fusion sources and technology for weapon effects simulation will meet ERDA requirements for an x-ray source with pulse width and exposure levels consistent with system threats to RV's. Present inertial confinement fusion electron accelerators operating in the bremsstrahlung mode are useful as x-ray simulation sources. For the far term, inertial confinement fusion sources operating with high gain pellets appear to be the only alternative to underground testing for hardening and synergistic effects.

APPENDIX A

REPRINTS OF PUBLISHED ARTICLES

1. M. M. Widner, F. C. Perry, L. P. Mix, J. Chang, and A. J. Toepfer, Jour. of Appl. Physics, 48, No. 3 (1977).

2. J. R. Asay, L. P. Mix, and F. C. Perry, Applied Physics Letters, 29, No. 5 (1976).

3. F. C. Perry and L. P. Mix, Applied Physics Letters, 27, No. 4 (1975).

4. F. C. Perry and L. P. Mix, Applied Physics Letters, 24, No. 12 (1974).

5. L. P. Mix and F. C. Perry, Jour. of Appl. Physics, 45, No. 7 (1974).

6. F. C. Perry and M. M. Widner, Applied Physics Letters, 29, No. 5 (1976).

7. F. C. Perry and M. M. Widner, Jour. of Appl. Physics, 47, No. 1 (1976).

Implosion dynamics of a hemispherical target irradiated by an intense relativistic electron beam*

M. M. Widner, F. C. Perry, L. P. Mix, J. Chang, and A. J. Toepfer

Sandia Laboratories, Albuquerque, New Mexico 87115
(Received 14 October 1976)

An intense tightly pinched relativistic electron beam from the Hydra accelerator (250 kA, 800 kV, 80 nsec) was used to produce an ablation driven implosion of a dense hemispherical shell. A laser reflection measurement was used to measure the implosion time and the velocity of the jet of material produced following the implosion. X-ray pinhole photography and optical holography were used to study the uniformity of target loading and ablator motion. Target dynamics was modeled by a two-dimensional Eulerian hydrodynamic code. The results indicated 17–50% of the total beam energy was delivered to the target, where the total beam energies varied between 17 and 20 kj. The uniformity in target loading varied between 20 and 80% from pole to equator. Suggestions are given for improving beam accuracy and target loading uniformity.

PACS numbers: 52.70.−m, 52.65.+z, 52.30.+r

I. INTRODUCTION

One method which has been proposed to achieve inertially confined thermonuclear fusion involves the use of high-power relativistic electron beams (REB's)[1,2] to implode spherical targets containing DT gas. The feasibility of irradiating millimeter size targets with both one and two beams has been demonstrated in recent experiments.[3–8] To investigate the feasibility of the two-beam approach as proposed in Ref. 1, it is relevant to study the dynamics of a hemispherical target irradiated by a single electron beam. In this paper, we present results from a series of experiments which were designed to study hemispherical targets irradiated by a single REB.

A new laser reflection technique[9] was employed to measure directly the interior target motion consisting of (a) the implosion time—the time for material to first reach the center of the hemisphere and (b) the jet velocity—the velocity of material produced on axis following the implosion. A two-dimensional Eulerian Hydrodynamic code was used to calculate these parameters. Where the implosion time and jet velocity were measured on a single electron beam shot, it is possible through the hydrodynamic analysis to obtain both the energy deposited in the hemisphere as well as the degree of loading uniformity. Independent data on deposition uniformity are provided by x-ray pinhole photography and optical holography of the blowoff plasma.

About 50 separate experiments were carried out with various diagnostics. Shot-to-shot variation of pinch location and focusing resulted in a 60% probability of striking the 4–5-mm-diam target within 3 mm of the axis, and the pinched beam FWHM varied between 4 and 6 mm. Six experiments were analyzed in detail. For these shots, results indicate 17–50% of the total beam energy was delivered to the target. Total beam energies were as large as 20 kJ. The bulk of the experiments indicated an 80% variation in beam intensity and target loading over the hemisphere, but a low of 20% nonuniformity was observed on one shot.

II. EXPERIMENTAL ARRANGEMENT AND DATA

A single line of the Hydra accelerator[10] was used to produce a pinched beam with intensity $\sim 10^{11}$–10^{12} W/cm^2 on a gold hemispherical shell target. The diode consisted of a 12.7-cm-diam cathode with a 2.54-cm hole in the center in which a 1-cm-diam hollow cylinder was located, extending 0.05 cm beyond the cathode face. Table I lists the beam parameters and diagnostics for a series of shots which will be analyzed below.

Time-integrated pinhole photography was obtained from side- and axial-looking pinhole cameras as shown in Fig. 1. In shots where other diagnostics were utilized, the use of one or both pinhole cameras was sometimes precluded. Centering of the beam pinch on target could be monitored with the axially looking pinhole camera. For a series of shots, the displacement of the axis of the pinched REB from the target axis was tabulated. Figure 2 illustrates the resulting statistics for pinch centering on target for a total of 30 experiments. The observed variation of pinch axial position from shot-to-shot can

TABLE I. Beam parameters and diagnostics.

Shot No.	d (cm)	V (kV)	I (kA)	Z (Ω)	$\int VI\,dt$ (kJ)	Diagnostics
1170	0.92	750	330	2.3	18	X-ray pinhole, holography
2666	1.3	950	280	3.4	20	X-ray pinhole
2669	1.2	800	270	3	17	X-ray pinhole
2798	1.4	950	300	3.2	17	Implosion time
2799	1.4	960	302	3.2	17	Implosion time
2971	1.3	830	250	3.3	20	Implosion time and jet velocity

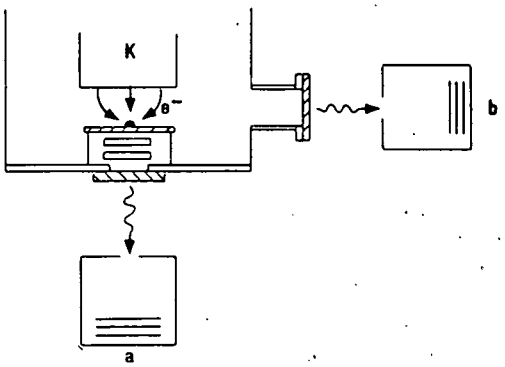

FIG. 1. Experimental arrangement showing x-ray pinhole camera placement.

be correlated with variations in anode and cathode planarity and alignment, as well as the geometry of the return current path. In the present experiments anodes were milled to 0.03-mm planarity and the anode-cathode gap typically varied by ≤ 0.2 mm over a diameter of 13 cm. Misalignments ≤ 0.2 mm led to wandering of the pinch off axis by ≤ 5 mm to the side of the diode where the gap was smaller. The effect of asymmetry in the return current flow was to distort the pinch.

Uniformity of target loading could be monitored on a shot-to-shot basis by the side-looking pinhole camera in Fig. 1. Data from shots Nos. 2666 and 2669 are shown in Fig. 3. In both these shots, the front-looking pinhole camera indicated good centering on target. The

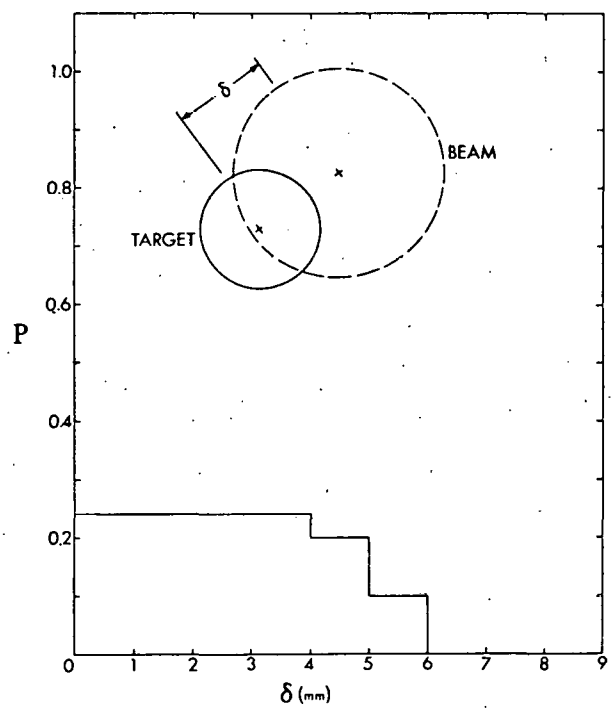

FIG. 2. Histogram showing displacement of beam axis from target axis for a hemispherical target mounted on a flat high-Z anode. Data is for a total of 30 shots.

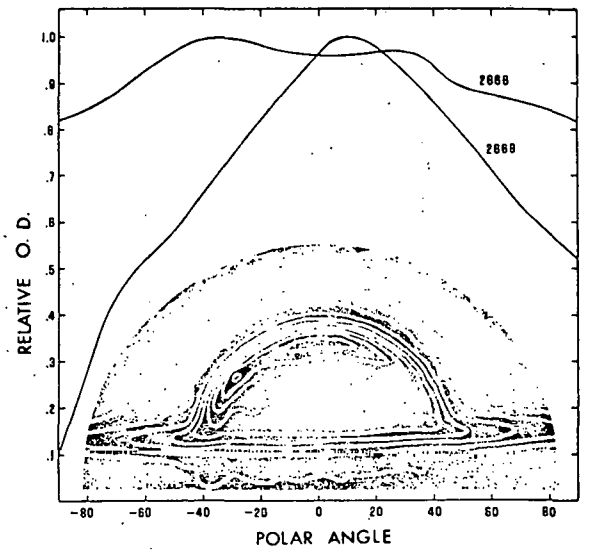

FIG. 3. Optical density versus polar angle for two shots on 4-mm-diam gold hemispheres. Inset shows pinhole-photo photograph for shot No. 2666. White lines follow contours of equal optical density.

pinhole photographs were digitally processed, corrected for spatial aberrations due to x-ray penetration of the pinhole edges and finite pinhole size, and were restored using an optimum Wiener filter at eliminate noise due to film graininess.[11] The inset in Fig. 3 is a restored photograph of an irradiated hemishell target showing contours of equal optical density for shot No. 2666.

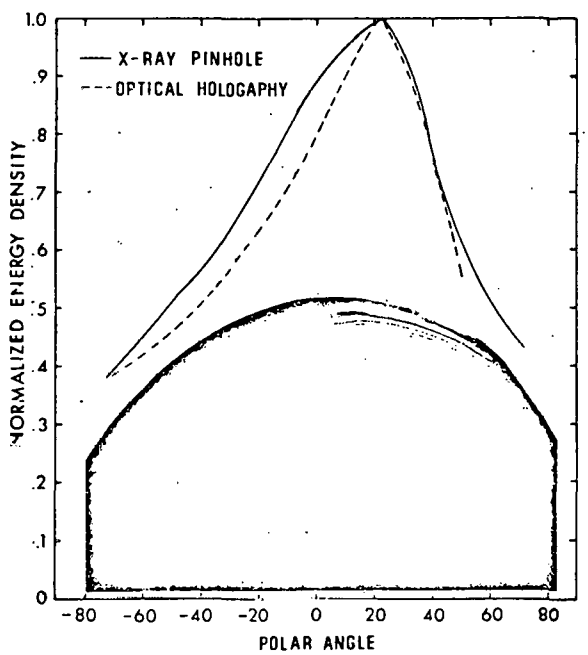

FIG. 4. Relative energy density versus polar angle as determined from optical holography. Inset shows hologram of irradiated hemisphere. One fringe corresponds to $\int n_e dl = 3.2 \times 10^{17}$ cm^{-2}.

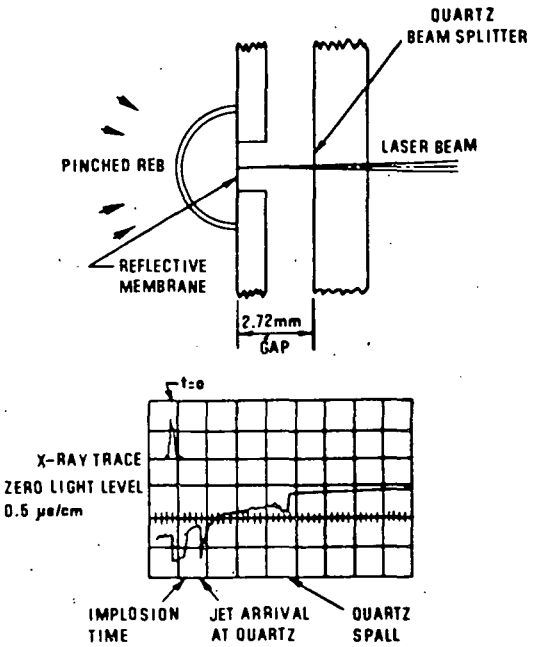

FIG. 5. Diagram of the target beam-splitter assembly and the data trace for shot No. 2971.

(The curves labeled by shot number correspond to target loading as a function of angle over the target surface.) For the exposures and film utilized, film calibration indicates that the optical density is directly proportional to exposure.[12] It is seen that the variation in target loading from shot-to-shot can be appreciable for similar diode operating parameters. However, analysis of five of the six shots in Table I indicates a 50–80% variation from pole to equator in beam energy deposition, as shown for shot No. 2669 in Fig. 3.

Uniformity of target irradiation can also be determined from holographic interferometry[13] of the target blowoff. Figure 4 shows a hologram of an irradiated target (Hydra shot No. 1170), taken using a 3-nsec pulse length PTM ruby laser. This hologram was made at the end of the beam power pulse, 110 nsec after the onset of diode current and ≈ 80 nsec after convergence of the pinched beam onto the target. Abel inversion of the fringe shift pattern, assuming the major contribution to the refractive index of the blowoff is due to free electrons, shows

$$n_e(r) = n_0 \exp(-r/\lambda),$$

where $\lambda = 0.032 \pm 0.008$ cm over the density range $3\times10^{18} \leq n_e(r) \leq 2\times10^{19}$ cm^{-3}. The velocity of the blowoff (1–2 cm/μsec) can be shown to be proportional to the square root of the energy/unit mass ϵ deposited in the front surface of the target,[14] which can in turn be correlated with the bremsstrahlung intensity as measured in the pinhole photographs. The normalized variation in ϵ over the target surface for the hologram is also shown in Fig. 4, assuming $v_{exp} \propto \epsilon^{1/2}$, and is consistent with the x-ray pinhole photography data for the same shot as shown. This result establishes a direct correlation between uniformity of target loading as observed with x-ray pinhole photography, and inferred from ablator motion using optical holography.

Radial density profiles at large angles to the diode axis ($\theta \geq 60°$) show a steplike behavior at large radii (> 0.5 cm). This is probably due to a contribution from the plasma expanding off the surface of the flat anode. The presence of a dense high-Z plasma in the region of the target equator probably leads to enhanced beam scattering and reduced loading as observed near the anode plane.

It is also possible that there is some interaction of the expanding plasma with the magnetic field of the electron beam.[15] If approximately one-half the total beam current flows inside a radius < 4 mm, than at the time the holograph was taken, $I = 390$ kA and the mganetic field pressure at a radius of 4 mm from the diode axis would be $\sim 10^8$ dyn/cm^3. For a gold plasma with ion density $\approx 10^{17}$ cm^{-3} and a velocity of $u \approx 2$ cm/μsec, the kinetic pressure is $\frac{1}{2}\rho v^2 \approx 10^8$ dyn/cm^3. Hence, at radii $\gtrsim 4$ mm from the diode axis, the blowoff kinetic pressure and magnetic pressure may be comparable. Although magnetic pressure plays a minor role in modifying the ablator motion in present experiments, at the beam current levels considered for breakeven targets[16] magnetohydrodynamic effects may dominate the ablator dynamics.

The experimental arrangement for the laser reflection experiment is shown in Fig. 5. The target has an outside radius of 2 mm and thickness 0.25 mm and was mounted on a 1.1-mm-thick copper anode plate over a cylindrical hole 1.5 mm in diameter. A 0.025-mm-thick aluminized Mylar membrane, which provided a reflecting surface for the laser beam incident from the rear, was mounted at the base of the target. At a distance of 2.72 mm from the membrane was the front reflecting surface of a beam-splitter mirror, which also reflected a portion of the laser light. As the target imploded to the center, the Mylar membrane was destroyed with a resulting loss of that portion of the reflected laser signal. Subsequently, the jet of material which was produced, moved axially and impacted the beam-splitter mirror with a resulting change in light intensity. In the case where the impact was sufficiently weak, a loss of reflected light occurred due to destruction of the reflecting surface. When the impact was strong, a burst of shock-induced luminescence was produced. In either case, the arrival time of the material at the beam splitter was recorded.

The data trace for shot No. 2971 is also shown in Fig. 5. A dual-beam oscilloscope recorded the PIN x-ray detector signal (upper trace) and a photomultiplier signal of the reflected light intensity (lower trace). The data was corrected for differences in cable delay time. The sharp peak in the PIN x-ray signal was chosen as the reference time ($t = 0$) in both the experiment and in the calculations. In the lower trace, the implosion time was sharply defined when the first loss in intensity occurred and the arrrival time at the beam splitter when the burst of shock-induced luminescence occurred.[9] An additional piece of data, which is not analyzed here, was the further loss in intensity occuring when the shock arrived at the rear surface of the beam splitter. Table II is a summary of the laser reflection data consisting

TABLE II. Summary of experimental data. There is an uncertainty of about ± 15 nsec in the times.

Shot	Implosion time (nsec)	Time to beam splitter (nsec)	Beam-splitter gap (mm)
2798	354	...	...
2799	305	...	...
2971	232	489	2.72

of three shots, all of which used gold hemispherical shell targets with a 2-mm outside radius and a 0.25-mm shell thickness. The first two shots only measured the implosion time since the beam-splitter mirror was not used. All of these data will be analyzed in Sec. III, with emphasis given to the last shot No. 2971.

III. CALCULATIONAL MODEL

The two-dimensional Eulerian hydrodynamic code CSQ[17] was used to calculate the target dynamics. The CSQ code contains a complete material equation-of-state with multiple materials including material phases, mixed phases, phase transitions, Saha equilibrium ionization model, elastic-plastic model, and a fracture model. The CSQ code has been previously used to study material response to REB's.[9,18] Cylindrical geometry is used with axisymmetry assumed. The electron beam deposition is included as an external energy source, with the total incident power on target $P_t(t)$ (W) given as

$$P(t) = V(t)I(t)F r_t^2/r_b^2(t),$$

where $V(t)$ is the diode voltage (V), $I(t)$ is the measured current (A), r_t is the initial target radius (cm), r_b is the pinch radius, and F is the fraction of the total beam current contained in the pinch. The pinch radius is chosen in accordance with the following time- and space-dependent beam pinching model:

$$r_b = r_c - v_p t' \quad \text{for } r_c - v_p t' > r_p$$

or

$$r_b = r_p \quad \text{for } r_c - v_p t' \leq r_p,$$

where r_c is the cathode radius, v_p is the pinch collapse velocity (cm/sec), and r_p is the final pinch radius. The time t' is measured from the beginning of the current rise. For the calculations here, we chose $r_p = r_t$ and $v_p = 10^8$ cm/sec which provided a pinch formation time which is in agreement with PIN array x-ray measurements.[19] The electron deposition, prior to pinching, does not noticeably affect the dynamic response, since the intensity is so low. Thus, the results were not sensitive to the details of the deposition model prior to pinching, but were sensitive to the choice of pinch-formation time. The incident power was further allowed to vary with the polar angle $\theta (0 \leq \theta \leq \frac{1}{2}\pi$, defined in Fig. 4) with the incident power P between angles θ_1 and θ_2

$$P = P_t \left[\int_{\theta_1}^{\theta_2} f(\theta)\sin(\theta)\,d\theta\right]\left[\int_0^{\pi/2} f(\theta)\sin(\theta)\,d\theta\right]^{-1},$$

where $f(\theta) = 1 + (2\theta/\pi)(R-1)$, $R = \text{const}$ is the ratio of the intensity at the equator to that at the pole ($0 \leq R \leq 1$). For the following calculations, the energy deposited on target and the deposition uniformity were selected by choosing F and R.

The in-depth deposition was assumed classical[9] with the profile computed using a separate one-dimensional electron transport code.[20] An isotropic angular distribution of incident electrons was assumed. As $V(t)$ changes, the deposition depth was adjusted in accordance with the appropriate voltage range table. A spherical source, similar to that used for one-dimensional target calculations,[16] was used with areal density computed along paths in the spherical radial direction toward the target center. Typically about 200 or more of such paths were used per deposition calculation, separated by equal increments in θ.

The computational accuracy was checked by comparing results for a spherical test problem with those obtained using a finer-zoned one-dimensional Lagrangian code[21] with the same equation-of-state. The test problem consisted of depositing 16 kJ over a 2-mm-radius gold spherical shell of thickness 0.25 mm in 80 nsec. The electron energy was 800 keV and a profile corresponding to an isotropic angular distribution was used. The Lagrangian code calculated an implosion time of 270 nsec. The calculated implosion time using CSQ differed by about 2% for the zone spacing of 0.04 mm which was also used for all the two-dimensional calculations reported here.

An example of one calculation is shown in Fig. 6. We used the experimentally measured voltage and current from the Hydra accelerator, and in this case chose $R = 0.5$ and E_a, the absorbed energy on target, = 6.9 kJ. Shown are cross-sectional plots of the target, anode, and beam splitter with the dot density proportional to the material mass density. The dots are used only for plotting and do not represent a fluid PIC calculation. As can be seen in the figure, energy was deposited only in the hemispherical shell and not in the copper anode plate. The first snapshot, at $t = 20$ nsec, shows the

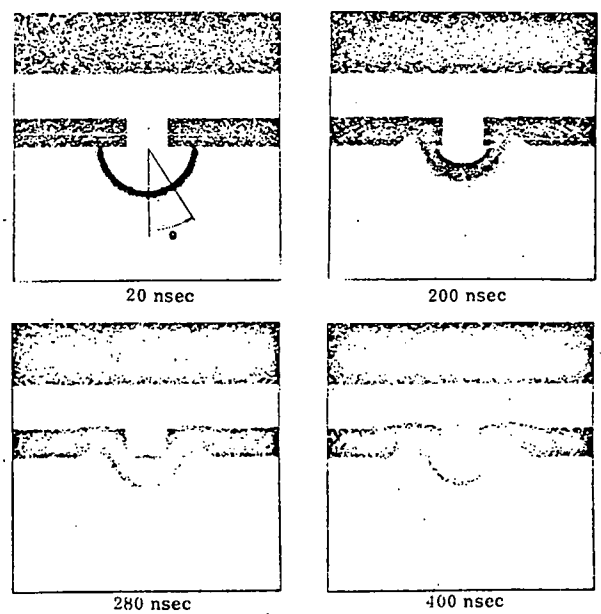

FIG. 6. Calculation of target implosion at several times showing the cross-sectional view of target density.

TABLE III. Summary of calculations.

Run	Energy deposited (kJ)	Intensity ratio (R)	Implosion time (nsec)	Jet velocity (cm/sec)
1	6.9	0.0	205	1.2×10^6
2	6.9	0.25	253	1.2×10^6
3	6.9	0.5	271	1.6×10^6
4	6.9	0.75	285	3.0×10^6
5	6.9	1.0	285	4.8×10^6
6	2.0	0.0	407	5.9×10^5
7	4.5	0.0	267	9.5×10^5
8	2.0	1.0	521	2.1×10^6
9	4.5	1.0	351	2.6×10^6
10	2.5	0.0	361	6.4×10^5
11	4.7	0.5	327	1.3×10^6
12	6.9	(Used expt. measured profile)	248	1.2×10^6

expanded ablator, which, in this case, consists of the outer portion of the gold target. The ablator thickness was approximately equal to the practical range for an 800-keV electron (0.19 g/cm^2). Also, a shock has traveled to the interior of the target shell and accelerated it inward. At 200 nsec, the target has traveled more than halfway to the center and the nonuniform interior shell position reflects the nonuniform loading. At 280 nsec, the imploding material has just passed the target center and at 400 nsec, a jet of material is streaming towards the beam splitter. Note that the anode plate has also responded to the target expansion; however, the rear surface velocity is much less than the jet velocity of the target and thus should not interfere with the measurement.

A large number of such calculations were made with different choices of R and E_a. These are summarized in Table III. The example in Fig. 6 corresponds to run No. 3 in Table III. Shown in Fig. 7 are plots of the position of the material surface on axis versus time for runs No. 1 through 5. Also shown on the same time scale is beam power pulse obtained from measured V and I for shot No. 2971. The peak in the power pulse corresponds to the peak in the PIN x-ray detector signal shown in Fig. 5, and defines the reference time for the calculations. The shock wave is seen to arrive at the shell interior at about $t=0$ for all the calculations. During the early phases of the implosion, the implosion velocity is nearly constant, while at later times the velocity increases as the material focuses near the target center. While the absorbed energy is constant for all these cases, the peak intensity is not and is largest for the case where $R=0$ for which the profile is strongly peaked on axis. The laser reflection data are also shown and appear most consistent with nonuniform loading with $R<0.25$. If we further parameterize the calculation results given in Table II with respect to R

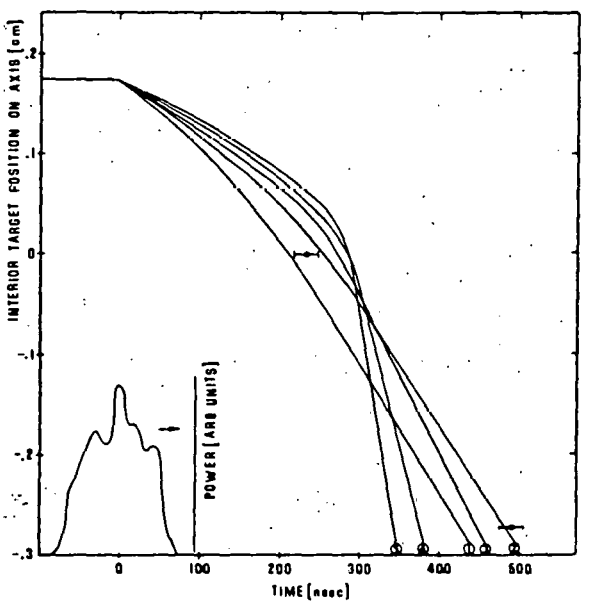

FIG. 7. Plots of interior target position on axis versus time for calculation runs No. 1–5. Also shown is the power pulse and the experimental data points for shot No. 2971 on the same time scales.

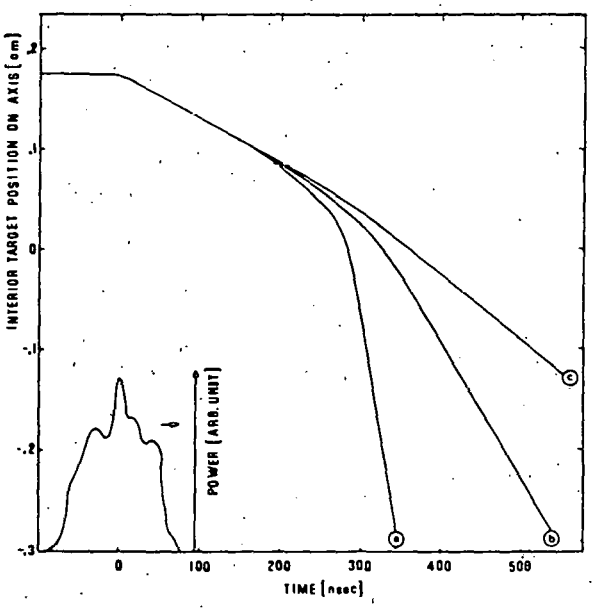

FIG. 8. Plots of interior target position on axis versus time for (a) run No. 5, (b) run No. 10, and (c) run No. 11.

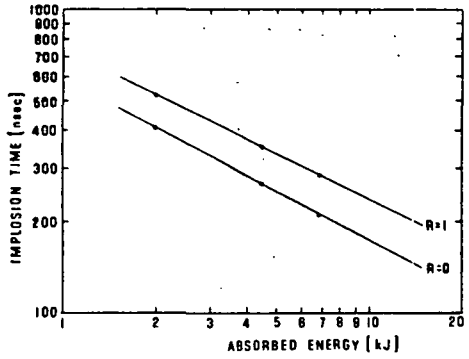

FIG. 9. Calculated implosion time versus absorbed energy for $R=0$, runs Nos. 1, 6, and 7 and for $R=1$, runs Nos. 5, 8, and 9.

and E_a, we find the best agreement for $5.1 \leq E_a \leq 6.8$ kJ and $R \lesssim 0.1$ for shot No. 2971. This is qualitatively consistent with the x-ray pinhole data shown in Fig. 2 for shot No. 2669 and the data for shot No. 1170 in Fig. 3.

Figure 8 shows another plot of material position versus time for three cases in which the intensity at the pole ($\theta=0$) was the same while the uniformity was different. Cases (a), (b), and (c) correspond to runs 5, 10, and 11 in Table III with $R=1$, 0.5, and 0, and with $E_a = 6.9$, 4.7, and 2.5 kJ, respectively. The response is seen to be essentially the same on axis during the early phases of the implosion. At later times, as the target material approaches the center, the curves separate as a result of different amounts of acceleration resulting from focusing. The amount of acceleration is proportional to the uniformity of loading. We deduce from these and other calculations then that the implosion time depends principally on the peak intensity on target, while the jet velocity depends strongly upon both the intensity and the loading uniformity. Also, the implosion time alone is not a sensitive measure of the total energy absorbed in the target as can be seen in Fig. 9.

Figure 9 plots implosion time versus absorbed energy for runs 1, 6, and 7 for $R=0$ and runs 5, 8, and 9 for $R=1$. These curves can be parameterized with $t_i \alpha E_a^{0.54}$ for $R=0$ and $t_i \alpha E_a^{0.5}$ for $R=1$. If we assume that $0 \leq R \leq 1$ represents the extremes in loading distributions, then for shot No. 2798, $2.4 \leq E_a \leq 4.8$ kJ and for shot No. 2799, $3.2 \leq E_a \leq 6.9$ kJ. The large uncertainty results from the uncertainty in loading uniformity which was not measured for these two shots. The total beam energy was only about 17 kJ for shots Nos. 2798 and 2799 (compared with 20 kJ for shot No. 2971) which may account, in part, for the longer implosion time.

Finally, we deviated from the previous profile shape to consider $f(0)=1$, $f(70°)=0.5$, and $f(90°)=0.1$ with linear variation in $f(\theta)$ between the above points. This shape is somewhat more consistent with the holography and time-integrated x-ray pinhole data. The energy deposited was 6.9 kJ and the results are described in Table III, run No. 12. These calculation data are nearly the same as those for run No. 2 which is qualitatively consistent with the data for shot No. 2971.

IV. CONCLUSION

In the inertial confinement fusion concept described by Yonas *et al.*,[1] the ablation driven implosion of a spherical target by two relativistic electron beams was proposed. The feasibility of this approach has been previously demonstrated[4] and the experiments reported in this work are part of a systematic study to determine the physics of target dynamics and beam-target coupling upon which electron beam fusion is based.

In particular, the implosion dynamics of ablatively driven hemispherical targets irradiated by an intense REB have been studied. The uniformity of target loading has been determined by a measurement of material jet velocity, optical holography of the blowoff plasma, and pinhole photography of x-ray emission. The distribution (uniformity) of deposited energy was determined by comparing experimental implosion times and jet velocity with the results of a calculational model from target response. For these experiments 17–50% of the total beam energy was delivered to the target, which compares well with the total energy in the central portion of the focused beam. Total beam energies were as large as 20 kJ. The uniformity of energy deposition was as poor as 80% variation over the target surface for most cases, and as good as 20% in one case.

Recent calculations of target performance for low power levels corresponding to those achievable with the Hydra accelerator indicate that measurable thermonuclear yield requires target irradiation with uniformity within $\approx 2\%$.[22–25] The targets in the present experiments were mounted at the equator on thick copper anode plate. It is probable that the high angle of incidence of the beam electrons to the diode axis near the plane of the anode results in significant scattering of the beam from the dense anode blowoff near the target equator. This would result in reduced loading of the target near the anode plane. Solutions to this problem may be (a) to suspend the target at the equator in a thin low-Z membrane to reduce scattering or (b) to suspend the target on a stalk, thus allowing uniform irradiation with a single beam.[5] It should be pointed out, however, that the results of the present investigation along with those for previous single-beam irradiations of "spheres on stalks" suggest that improvements in deposition uniformity may be accompanied by reduced beam-target coupling.

Alignment of beam and target axes has been shown to be dependent on return current symmetry and anode-cathode planarity and alignment. For very large diameter cathodes, it may be necessary to inject a low-density stream of plasma on axis to define an axis of symmetry. Past experiments have shown[26–28] that beam centering can be improved by this technique.

ACKNOWLEDGMENT

The authors would like to acknowledge helpful discussions with J.R. Freeman and G. Yonas, and computational assistance provided by Mrs. Lessie Lee.

*Work supported by the U.S. Energy, Research and Development Administration, under Contract AT(29-1)-789.

[1]G. Yonas, J.W. Poukey, K.R. Prestwich, J.R. Freeman, A.J. Toepfer, and M.J. Clauser, Nucl. Fusion 14, 731 (1974).
[2]M.V. Babykin, E.K. Zavoiskii, A.A. Ivanov, and L.I. Rudakov, *Proc. 4th Int. Conf. Plasma Physics and Controlled Fusion* (IAEA, Vienna, 1971), Vol. 1, p. 635.
[3]A.J. Toepfer, *Annals of the New York of Sciences Conference on Electrostatic and Electromagnetic Confinement of Plasmas and Phenomenology of Relativistic Electron Beams* (New York Academy of Sciences, 1975), Vol. 251, p. 609.
[4]J. Chang, M.J. Clauser, J.R. Freeman, G.R. Hadley, J.A. Halbleib, D.L. Johnson, J.G. Kelly, G.W. Kuswa, T.H. Martin, P.A. Miller, L.P. Mix, F.C. Perry, J.W. Poukey, K.R. Prestwich, S.L. Shope, D.W. Swain, A.J. Toepfer, W.H. Vandevender, M.M. Widner, T.P. Wright, and G. Yonas, Proceedings of the Fifth Conference on Plasma Physics and Controlled Nuclear Fusion Research, Toyko, 1974, Vol. 2, p. 347 (unpublished).
[5]J. Chang, M.M. Widner, G.W. Kuswa, and G. Yonas, Phys. Rev. Lett. 34, 1266 (1975).
[6]M.J. Clauser, J.R. Freeman, S.A. Goldstein, G.R. Hadley, J.A. Halbleib, J.G. Kelly, G.W. Kuswa, C.W. Mendel, P.A. Miller, L.P. Mix, F.C. Perry, J.W. Poukey, S.L. Shope, D.W. Swain, M.A. Sweeney, A.J. Toepfer, W.H. Vandevender, M.M. Widner, T.P. Wright, G. Yonas, K.D. Bergeron, and J. Chang, *Proceedings of the 7th European Conference on Controlled on Controlled Fusion and Plasma Physics* (CRPP, Ecole Polytechnique Federale de Lausanne, Switzerland, 1975), p. 85.
[7]E.I. Baranchikov, A.V. Gordeev, U.V. Koba, V.D. Korolev, V.S. Pen'kina, L.I. Rudakov, V.P. Smirnov, A.D. Sukhov, and E.Z. Tarumov, Proceedings of the First International Topical Conference on Electron Beam Research and Technology, Albuquerque, N.M., 1975, Vol. I, p. 284 (unpublished).
[8]J. Chang, L.P. Mix, F.C. Perry, M.M. Widner, and J.W. Poukey, in Ref. 7, p. 82.
[9]F.C. Perry and M.M. Widner, Bull. Am. Phys. Soc. 20, 1272 (1975); a similar technique was used previously to study electron deposition. F.C. Perry and M.M. Widner, J. Appl. Phys. 47, 127 (1976).
[10]T.H. Martin, IEEE Trans. Nucl. Sci. NS-20, 289 (1973).
[11]A.J. Toepfer and H.B. Demuth (unpublished).
[12]J.K. Silk and R. Simon, *A Study of the Response of Photographic Film to Beam-Target X-rays*, ASE-3869 (American Science and Engineering, Cambridge, Mass., 1976).
[13]L.P. Mix, J.G. Kelly, G.W. Kuswa, D.W. Swain, and J.N. Olsen, J. Vac. Sci. Technol. 10, 951 (1973).
[14]M.J. Clauser (private communication).
[15]G. Bekefi, T.J. Orzechowski, and K.D. Bergeron, in Ref. 7, p. 303.
[16]M.J. Clauser, Phys. Rev. Lett. 34 570 (1975).
[17]S.L. Thompson, Sandia Laboratories Report SAND 74-0122, 1975 (unpublished).
[18]M.M. Widner and S.L. Thompson, Sandia Laboratories Report SAND 74-351, 1974 (unpublished).
[19]L.P. Mix and J. Chang, Bull. Am. Phys. Soc. 20, 583 (1975).
[20]M.J. Berger and S.M. Seltzer, National Bureau of Standards Reports No. 9836 and No. 9837, 1968 (unpublished); and J.A. Halbleib, Sr., and W.H. Vandevender, Sandia Laboratories Report SC-DR-71-0598, 1971 (unpublished).
[21]S.L. Thompson, Sandia Laboratories Report SLA-73-0477, 1973 (unpublished), and references to the CHARTD code contained therein.
[22]D.J. Meeker, J.H. Nuckolls, and R.O. Bangerter, Bull. Am. Phys. Soc. 20, 1352 (1975).
[23]W.P. Gula and R.C. Kirkpatrick, in Ref. 7, p. 158.
[24]M.J. Clauser, Sandia Laboratories Report SAND-76-0158, 1976 (unpublished).
[25]M.A. Sweeney (unpublished).
[26]G. Yonas, K.R. Prestwich, J.W. Poukey, and J.R. Freeman, Phys. Rev. Lett. 30, 164 (1973).
[27]P.A. Miller, J. Chang, and G.W. Kuswa, Appl. Phys. Lett. 23, 423 (1973).
[28]P.A. Miller, J.W. Poukey, and T.P. Wright, Phys. Rev. Lett. 35, 940 (1975).

Ejection of material from shocked surfaces*

J. R. Asay, L. P. Mix, and F. C. Perry

Sandia Laboratories, Albuquerque, New Mexico 87115
(Received 12 May 1976)

Velocity interferometry and double-pulse holography have been used to study material ejected from surfaces which are impulsively loaded with plane shock waves. Experiments performed on aluminum shocked to 25 GPa (250 kbar) provide the average mass and velocity distribution as well as the spatial distribution of material ejected from the surface. A total mass of about 3 $\mu g/cm^2$ was ejected when the shock arrived at the surface in the present experiments, and a substantial part of this material resulted from jetting at small pits on the surface.

PACS numbers: 62.50.+p, 79.90.+b, 42.40.Kw

It is well known that the reflection of strong shock waves from surfaces can cause either the development of Rayleigh-Taylor instabilities at material interfaces[1,2] or jetting of material from surfaces.[3–6] However, very little is known about physical mechanisms which are important in the degradation of surfaces during shock loading. In this paper, we present a technique which should prove to be useful for evaluating the ejection of material from shocked surfaces. The technique allows quantitative measurements of the mass-velocity distribution of ejecta and also a measure of its spatial distribution. The latter information is especially useful for studying physical mechanisms which influence the ejection of mass.

It has been observed in previous investigations that when a shock arrives at a free surface, material can be ejected in the form of a fine spray.[3,4] A common technique previously employed to study the motion of this spray has been fast streak and framing photography.[4] With these methods, it is difficult, if not impossible, to deduce information about the mass or velocity distribution of ejected material. In addition, the spatial resolution obtained previously has generally been inadequate to reveal structure of ejecta on the scale of a few microns. Both of these features can now be investigated with the technique described here, and the method has been used to obtain the first measurements of the spatial and velocity distribution of material ejected from aluminum surfaces during shock loading.

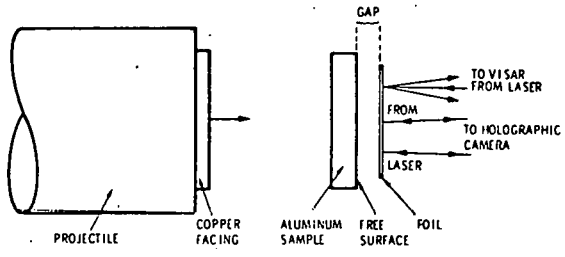

FIG. 1. Schematic illustration of the technique used to produce plane shock waves in a specimen. The copper facing and aluminum specimen thicknesses in the present experiments were on the order of 0.3 and 0.4 cm, respectively. Either aluminum or cellulose acetate was used as foils. For the cellulose acetate foils, a 120-nm-thick spectral aluminum reflector was vapor deposited on the rear surface.

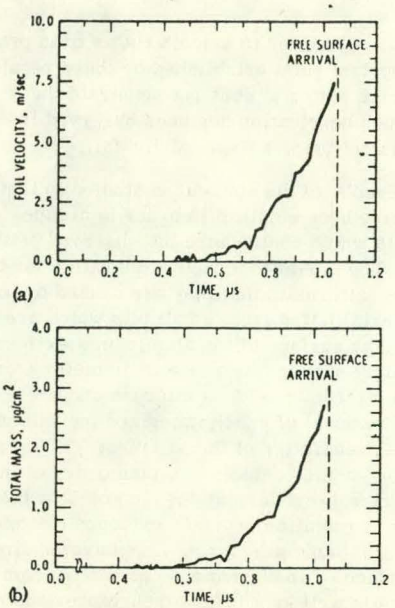

FIG. 2. Results of a VISAR experiment obtained on an aluminum foil, 4.3 μm thick, and separated by 2.74 mm from the aluminum free surface. (a) Foil velocity as a function of time after impact at the free surface of the specimen ($t = 0$). (b) The corresponding total mass accumulated on the foil.

The basic experimental configuration is shown schematically in Fig. 1. Plane shock waves in aluminum were produced by impact of a projectile accelerated with a high-velocity gun.[7] After shock arrival at the rear surface of the aluminum specimen, material ejected from the surface was detected by impeding it with a foil after propagation across a carefully measured gap. The time at which mass arrived at the foil, the particle velocity of the foil, and the local microscopic deformations of the foil were then precisely measured. Two interferometry systems have been used for this purpose. One is a diffuse surface velocity interferometer[8] (VISAR) which allows a continuous measurement of the arrival time of ejected mass and the particle velocity of the foil. In this technique reflected light from a focused laser beam of ~0.1 mm diameter on the foil is used as incident light to a velocity interferometer.[8] The fringe shift produced in the interferometer is proportional to the particle velocity of the foil. The second interferometer used in this work was a double-pulse holographic system[9] which produced a series of four holographic exposures with a time separation of 16 nsec during the foil motion. Interference of these exposures with a corresponding set taken before the experiment allowed a time-resolved fringe record of the local deformations of the foil. These local deformations were then used to deduce the spatial distribution of mass arriving at the foil. The area on the foil observed with this system was about 6 mm in diameter. The precision in velocity obtainable with the VISAR is about ± 0.2 m/sec, while the spatial resolution of the holographic system is about 20 μm.

In principle, the VISAR and holographic systems can be combined in a given experiment to provide all of the data necessary to determine the parameters discussed earlier and this has been accomplished on a number of experiments. However, the best results to date have been attained under conditions which optimized the capabilities of each system in a given experiment. Since the VISAR experiments were designed to determine the average response of the foil, it was necessary that the foil separation be sufficiently large to smooth out any structure of the ejecta. In contrast, it was necessary to maintain close separations in the holographic experiments, since these experiments were designed to detect the spatial resolution of the ejected mass. Thus, these different requirements indicate separate experiments. The best VISAR experiments have been obtained from diffusely reflecting 4-μm-thick aluminum foils separated from the surface by about 3 mm. On the other hand, the best holographic results have been obtained with specularly reflecting 8-μm-thick cellulose acetate pellicles[10] separated by about 0.5 mm from the free surface.

The velocity history of the foil measured with the VISAR can be used to determine the mass and velocity of ejecta arriving at the foil if certain assumptions are made. The major assumptions necessary to reduce these data are that (i) all mass is ejected instantaneously when the shock arrives at the free surface; (ii) inelastic collision with the foil is obtained, with no penetration through the foil, (iii) the spatial distribution of ejected mass is sufficiently fine so as to be essentially continuous over the area recorded by the interferometer; and (iv) the foil can be treated as a rigid body during its motion. Under these assumptions, the ejected mass per unit area, m, accumulated on the foil can be determined from the conservation of momentum, which results in the approximate relation

$$\frac{dm}{dt} \doteq \frac{M}{v}\frac{dV}{dt},$$

where M is the areal density of the foil (~1.2 mg/cm^2 in the present experiments), v is the velocity of the ejected mass, and V is the foil velocity. Assumptions (iii) and (iv) would not be valid if the foil were close enough to the surface to experience highly localized deformations. However, data taken to date for various foils and separations indicate that these assumptions are reasonable under the conditions employed in the present experiments.

Two experimental results are reported which illustrate the capabilities of the technique. the nominal shock pressure obtained in each case was 25 GPa (250 kbar), with resulting free surface velocities of 2.6 km/sec and surface accelerations of at least 10^3 km/sec^2. The specimen free surface in each case was polished to a specular finish with 1-μm diamond paste and then rf sputtered to remove any residual impurities on the surface.

Figure 2 shows the results of a VISAR experiment conducted on an aluminum foil separated from the free surface by 2.74 mm. The measured foil velocity in Fig. 2(a) illustrates that significant motion of the foil is obtained before impact by the free surface which occurs at 1.04 μsec. The first ejecta to arrive at the

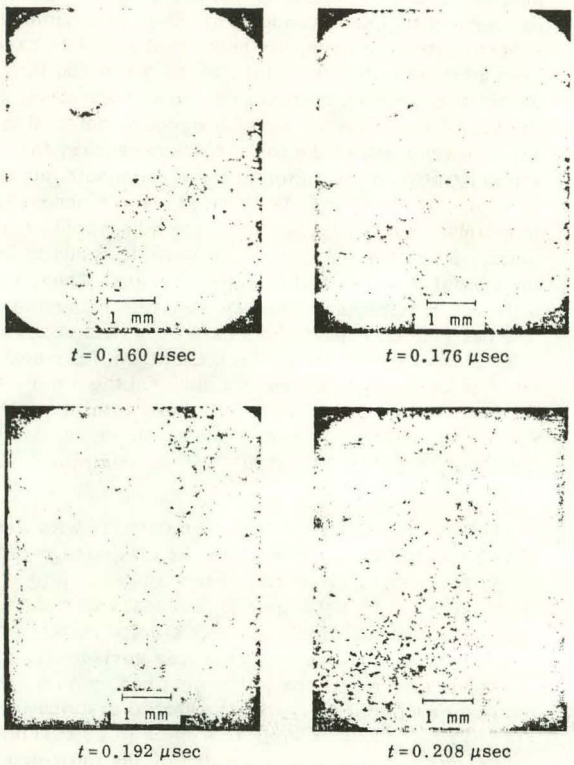

$t = 0.160$ μsec $t = 0.176$ μsec

$t = 0.192$ μsec $t = 0.208$ μsec

FIG. 3. Interference holograms of the surface of a cellulose acetate foil separated by 0.61 mm from the free surface of an aluminum specimen. The time origin is taken to coincide with shock arrival at the free surface of the specimen and impact with the foil occurs at 0.23 μsec.

foil have a velocity of about 7 km/sec, which is about 2.5 times larger than the free surface velocity of 2.6 km/sec. From the relation above, the data shown in Fig. 2(a) allow a determination of the ejected mass arriving at the foil as a function of time, which is shown in Fig. 2(b). As illustrated by the figure, a total of about 3 $\mu g/cm^2$ is ejected from the surface of the specimen in this experiment. The absolute accuracy of ejected mass which can be determined is estimated to be about ± 0.5 $\mu g/cm^2$, although changes in mass approximately an order of magnitude smaller can be detected.

Figure 3 illustrates the result of an experiment obtained with the holographic technique. In this figure fringe records are shown which were reconstructed from four holograms taken during the motion of a cellulose acetate pellicle separated from the free surface by 0.61 mm. The origin of time ($t = 0$) is taken to coincide with shock arrival at the free surface. Simultaneous VISAR measurements indicated that the first mass ejected from the free surface in this experiment arrived at the foil at 0.07 μsec and that free surface impact occurred at approximately 0.23 μsec.

The most prominent features of these records are the small circular fringe patterns which represent small protruding deformations of the pellicle. Such deformations could be formed by small particles or microjets impinging on the pellicle. Most of these microscopic deformations are observed to smooth out as time proceeds. An important point established by these results is that the ejected material does not penetrate the 8-μm pellicle, although penetration has been observed in another experiment using a 6-μm Mylar foil.

Photomicrographs of the specimens studied in these experiments have been obtained in order to deduce physical defects which could cause the observed pellicle deformations. The most reasonable explanation for the circular fringe patterns is that they are caused by impact from material jetted from small pits which are observed on the free surface of the aluminum specimens. These irregularly shaped pits range in diameter from a fraction of a micron to several microns and are formed by the removal of precipitates and inclusions during surface preparation of the samples. The areal density of these surface defects is on the order of the density of the circular deformations observed on the foil. Thus this correlation provides evidence that material may jet from these pits during impulsive loading of the free surface. The phenomenon of jetting from shaped cavities is well known,[3,4] although previous experimental work on jetting has been performed on cavities with dimensions 4—5 orders of magnitude larger than the pits observed here. Nevertheless, maximum jet velocities observed in the present experiments are compatible with predictions of the steady-state theory for jet formation.[3]

In addition to the circular deformations, the fringe records in Fig. 3 indicate additional local deformations occurring on the foil. These include the large nearly straight fringes observable on the fringe records in Fig. 3 and some very fine fringes with spacings on the order of tens of microns, which are not observable in the reproductions shown in Fig. 3. The mechanisms responsible for these effects are not presently understood. However, it has been suggested that microjetting can occur at many different surface defects such as scratches, tool marks, subsurface inclusions,[4] or from crystal imperfections such as grain boundaries and slip bands. One or more of these mechanisms could contribute to the total mass ejected in these experiments, although the present data are not sufficient to unambiguously identify any of these additional effects.

In conclusion, the combined interferometer techniques presented here provide powerful tools for studying the effects of microjetting from surfaces during shock loading. The VISAR allows precise measurement of the velocity history of a secondary foil separated from the free surface and, therefore, a quantitative evaluation of the mass and velocity of material ejected from the surface. The pulsed holographic technique provides complementary information regarding the local foil deformations, which therefore allows an estimation of the spatial distribution of ejecta. The combined information is extremely useful for deducing the relative importance of different physical mechanisms which influence the ejection of mass from shocked surfaces. Data obtained with these two techniques in the present experiments indicate that approximately 3 $\mu g/cm^2$ is ejected from an aluminum surface shocked to 25 GPa. Over this range of pressure the

results indicate that a substantial part of the ejection occurs at small pits on the surface.

The authors would like to express their appreciation to R. Kessler, D.B. Baldwin, C. Konrad, A. Jones, and B. Hardy for their assistance in various aspects of these experiments. Valuable discussions were also held with D. Venable of Los Alamos Scientific Laboratory during the course of this work.

*Work supported by the U. S. Energy Research and Development Administration, ERDA.

[1]J.D. Lindl and W.C. Mead, Phys. Rev. Lett. 34, 1273 (1975).

[2]F.C. Perry and L.P. Mix, Appl. Phys. Lett. 27, 194 (1975).

[3]J.M. Walsh, R.G. Shreffler, and F.J. Willig, J. Appl. Phys. 24, 349 (1953).

[4]D. Venable (private communication).

[5]F.C. Perry and M. Widner, J. Appl. Phys. 47, 127 (1976).

[6]J.R. Asay and L.M. Barker, J. Appl. Phys. 45, 2540 (1974).

[7]R.P. May, SC-RR-72-0180, 1972 (unpublished).

[8]L.M. Barker and R.E. Hollenbach, J. Appl. Phys. 43, 4669 (1972).

[9]L.P. Mix and R. Kessler, Rev. Sci. Instrum. (to be published).

[10]The pellicle beam splitters used in this work were thin-film cellulose acetate membranes manufactured by National Photocolor Corp., South Norwalk, CT. A high-quality specular reflector was prepared on the film by vapor depositing a 120-nm aluminum mirror on one side.

Electron-beam-driven instability in a solid*

F. C. Perry and L. P. Mix

Sandia Laboratories, Albuquerque, New Mexico 87115
(Received 11 April 1975; in final form 2 June 1975)

A relativistic electron beam (REB) accelerator was used to generate a shock wave (6–10 kbar) in a solid aluminum plate, and the tensile wave following the compressive wave produced an instability of the back surface of the plate. The wavelength of the instability, observed by holographic interferometry, and the measured negative acceleration of the solid-gas interface were used in a modified theory of Taylor instability to determine a value of 1.7×10^3 P for the viscosity of aluminum which was in reasonable agreement with a previously reported value. It is suggested that the mechanism of Taylor instability can qualitatively explain the observation in a previous experiment of a distribution of particle velocities at a surface of a solid upon arrival of a very high-amplitude (~1 Mbar) shock wave.

PACS numbers: 62.50., 45.40.N, 52.75.D

It is of considerable interest[1] to investigate the role of dynamic material properties, e.g., the dynamic yield strength, tensile strength, and viscosity, in the development of hydrodynamic instabilities. In addition, such studies are relevant to experiments and calculations directed towards the goal of electron beam[2] or

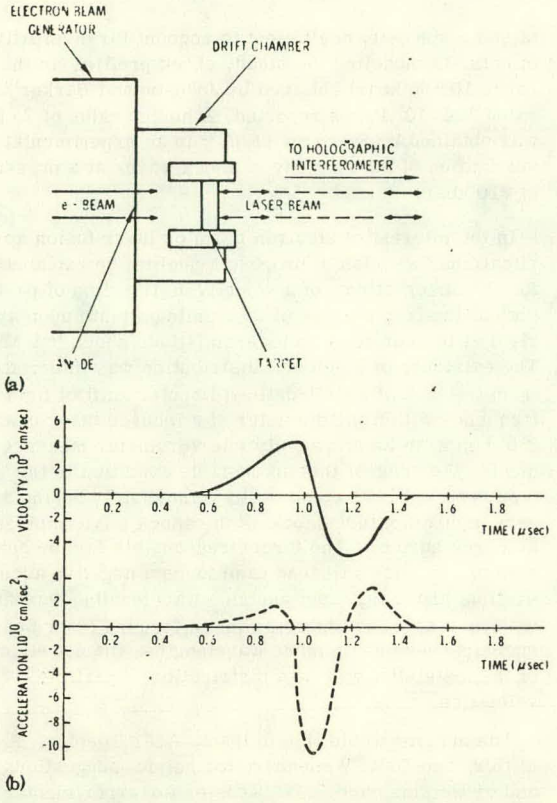

FIG. 1. (a) Experimental arrangement; (b) velocity and acceleration of the rear surface of an aluminum plate. The peak pressure generated was about 7.6 kbar.

laser[3] fusion by means of pellet implosion. In this paper we report on the first observation of an elastic-plastic instability or buckling of a solid-air interface where the acceleration of the interface arose from the arrival of a relief or tension wave generated by an intense electron beam pulse.

The experiment consisted of the following: a Febetron 705 electron beam generator with the nominal characteristics (energy ~1.5 MeV, current 6 kA, and a triangular pulse shape with ~100-nsec base width) was used to deliver beam fluences ~10 cal/cm^2 on to 6061-T6 aluminum targets. For these electrons the specific energy deposition E (energy/mass) is roughly 2 cal/g per cal/cm^2. Under the conditions of the experiment, a single electron beam pulse deposits energy in the aluminum in a time duration short enough that the material is inertially constrained. Thus, a stress pulse[4] with magnitude $\sigma = \rho\gamma E$, where γ is the Gruneisen parameter (~2) and ρ is the density (2.7 g/cm^3) is generated in the front part of the aluminum and propagates with amplitude $\frac{1}{2}\sigma$ to the rear of the target. From previous materials experiments, we know that the compression wave in aluminum behaves predominantly in a thermoelastic fashion and propagates in a state of uniaxial strain at the dilational wave speed. The Hugoniot elastic limit (HEL) for 6061-T6 aluminum is approximately 6 kbar and the experiments were in the range of 6—10 kbar. Therefore, some plastic yielding occurred. The release wave following the compressive wave at these stress levels has been shown[6] to be influenced by reverse plastic straining.

The dynamic response of the rear surface upon arrival of the stress wave was observed by the method of

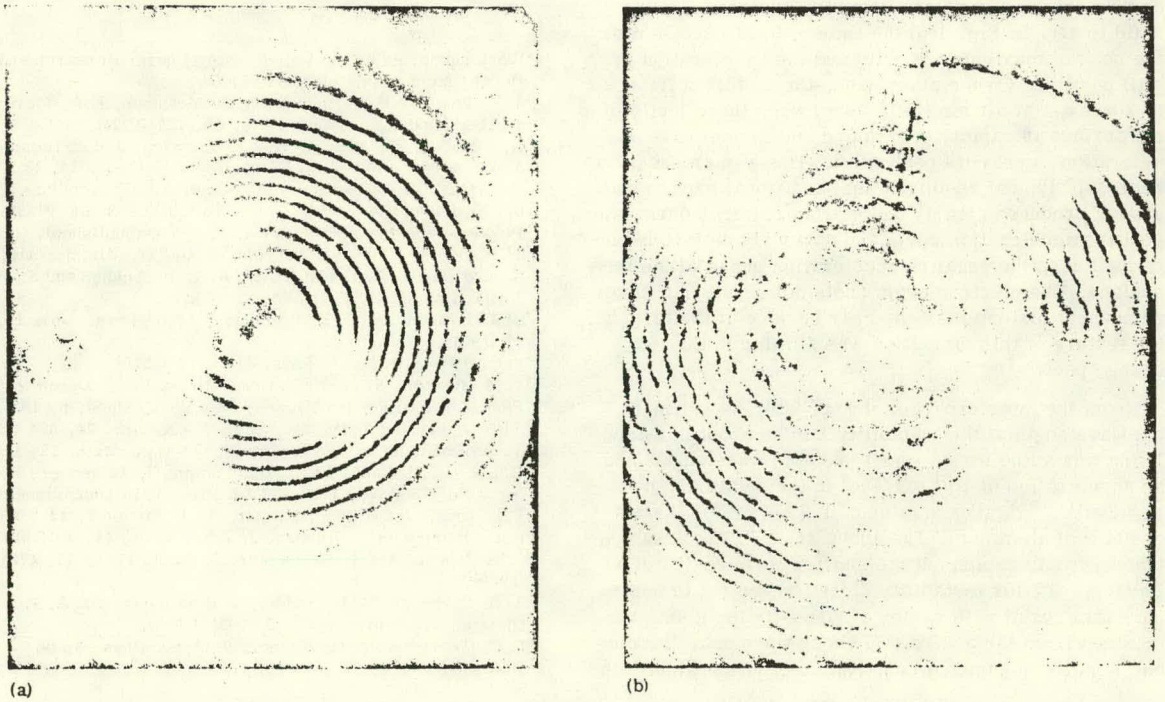

FIG. 2. Holographic interferograms of the rear surface of an aluminum plate of thickness 0.635 cm and diameter 5.08 cm at (a) 0.92 μsec and (b) 1.02 μsec after energy deposition. The scribe marks are 0.508 cm apart.

holographic interferometry.[7] The experimental arrangement is shown in Fig. 1(a). A PTM ruby laser with a pulse duration of about 3 nsec is fired twice for each electron beam pulse; first, before the electron beam pulse, and second at a selected time during the excursion of the rear surface. The fringe pattern obtained on the holographic plate gives the net displacement in the beam axis of the rear surface at the time of the second laser pulse. The laser pulse duration of 3 nsec was sufficiently short in these dynamic experiments to produce fringe patterns of good clarity.

The complete time histories of a point on the rear surface are shown in Fig. 1(b) for velocity and acceleration. The velocity time history was experimentally obtained in a previous study using laser velocity interferometry. A time of 0.99 μsec is required for the crossing of a dilatational wave from the front to the rear surface of the aluminum target. After that time the rear surface velocity decreases rapidly, thus causing negative acceleration. The acceleration profile was obtained by differentiating the velocity profile. For the shot illustrated in Fig. 1(b), one notes a peak negative acceleration of about 10^{11} cm/sec^2 lasting for a time duration less than 0.2 μsec.

The results of two shots employing holographic interferometry are illustrated in Fig. 2. The experimental conditions were the same for each of the shots except for the time of the second exposure of the holographic plates. In Fig. 2(a) the second exposure occurred 0.92 μsec after the beginning of the electron beam pulse, and in Fig. 2(b) the second exposure occurred 0.10 μsec later at 1.02 μsec after the electron pulse. The clear undistorted fringes of 2(a) are the result of the compressive wave accelerating the surface from the solid to air. In Fig. 1(b) the time of 0.92 μsec is near the peak of maximum velocity and the acceleration is still positive. On the other hand, the distorted fringes of 2(b) exist at a time (1.02 μsec) when the velocity of the surface is rapidly decreasing and the negative acceleration is near its peak value. These interferograms represent typical results in that additional experiments always produced clearly undistorted patterns during the positive acceleration cycle and obviously distorted patterns during the negative acceleration phase of the free surface. The electron beam shots did result in a small permanent distortion of the rear surface of the target; the texture of this distortion was similar to that of orange peel.

From the interferogram of Fig. 2(b), we estimate the wavelength of the instability λ to be about 0.1 cm. Using this value for λ_m (most unstable wavelength) and an acceleration of 10^{11} cm/sec^2 in the relationship[8] $\lambda_m = 2\pi a^{-1/3}\nu^{2/3}$ gives a value of 1.7×10^3 P for the viscosity ν of aluminum. The above relationship assumes that viscosity damps out the shorter wavelengths of a Rayleigh-Taylor instability. It is interesting to compare this result with values of viscosity for aluminum obtained from the analysis of shock wave data. Prieto and Renero[9] assumed a constitutive equation which contained a viscosity coefficient to account for dissipative effects. In modeling the steady shock profiles (in the range 10–90 kbar) obtained by Johnson and Barker[10] a value 1.4×10^3 P was reported. A higher value of 2×10^4 was obtained by Sakharov *et al.*[11] in an experimental investigation of the stability of shock waves at a pressure of 310 kbar.

In the interest of electron beam or laser fusion applications, we wish to propose a qualitative explanation for the observation[12] of a velocity distribution of particles at the free surface of an aluminum plate upon arrival at the surface of a high-amplitude shock (~1 Mbar). The existence of a velocity distribution was inferred from the lack of a well-defined Doppler shift of light frequency within the diameter of a focused laser beam (~0.1 mm) in laser velocity interferometer measurements. We suggest that an unstable condition of the type reported here could occur immediately behind a very high-amplitude shock as the shock wave impinges at a free surface. The forces responsible for the cohesion of particles will tend to produce a negative acceleration; and if the most unstable wavelengths decrease with increasing pressure so that a focused laser beam encompasses one or more wavelengths, the net effect of the instability will be a distribution of particle velocities.

The authors would like to thank A.J. Toepfer, P.A. Miller, and D.L. Wesenberg for helpful suggestions and criticisms, and R.W. Kessler for experimental assistance. J.N. Johnson of Terra Tech Company also offered many helpful suggestions.

*Work supported by the United States Energy Research and Development Administration, ERDA.

[1] J.F. Barnes, P.J. Blewett, R.G. McQueen, K.A. Meyer, and D. Venable, J. Appl. Phys. 45, 727 (1974).
[2] G. Yonas, J.W. Poukey, K.R. Prestwich, J.R. Freeman, A.J. Toepfer, and M.J. Clauser, Nucl. Fusion 14, No. 5 (1974); L.I. Rudakov and A.A. Samarsky, Proceedings of the 6th European Conference on Controlled Fusion and Plasma Physics, Moscow, USSR, 1973, p. 487 (unpublished).
[3] J. Nuckolls, L. Wood, A. Thiessen and G. Zimmerman, Nature (Lond.) 239, 139 (1972); K.A. Brueckner and S. Jorna, Rev. Mod. Phys. 46, 325 (1974).
[4] R.A. Graham and R.E. Hutchison, Appl. Phys. Lett. 11, 69 (1967).
[5] F.C. Perry, J. Appl. Phys. 41, 5017 (1970).
[6] L.M. Barker, *Behavior of Dense Media Under Dynamic Pressure* (Gordon and Breach, New York, 1968), p. 483.
[7] F.C. Perry and L.P. Mix, Appl. Phys. Lett. 24, 624 (1974).
[8] R. Bellman and R.H. Pennington, Q. Appl. Math. 12, 151 (1954); G. Birkhoff, Los Alamos Scientific Laboratory Reports No. LA 1862, 1955 and LA 1972, 1956 (unpublished); T.S. Green and G.B.F. Niblett, Nucl. Fusion 1, 42 (1960).
[9] F.E. Prieto and C. Renero, J. Appl. Phys. 44, 4013 (1973).
[10] J.N. Johnson and L.M. Barker, J. Appl. Phys. 40, 4321 (1969).
[11] A.D. Sakharov, R.M. Zaidel, V.N. Mineev, and A.G. Oleinik, Sov. Phys.-Dokl. 9, 1091 (1965).
[12] F.C. Perry and M.M. Widner, J. Appl. Phys. (to be published).

Application of holographic interferometry to shock waves in solids*

F. C. Perry

Applied Material Science Division 5323, Sandia Laboratories, Albuquerque, New Mexico 87115

L. P. Mix

Electron Beam Physics Division 5242, Sandia Laboratories, Albuquerque, New Mexico 87115

(Received 2 November 1973)

Double-pulse holographic interferometry has been used to determine the rear-surface displacement of a target exposed to a pulsed electron beam. The technique has been applied to the study of shock-wave propagation in a complex heterogeneous material—three-dimensional quartz phenolic. The results suggest a multiple-wave character for shock propagation in this material.

Very intense pulsed electron beams (tens of nanoseconds and thousands of Amperes) have been previously used to generate shock waves in materials.[1] Measurements of material response have ordinarily been performed with laser interferometers[1,2] and piezoelectric gauges,[3] where experimental data consisted of stress, displacement, or velocity time histories at a single point (or over a small area). Purposes of such experiments have been the determination of Grüneisen parameters and dynamic response over a wide range of internal energies, and analyses of data have generally included the assumptions of one-dimensional response.

The application of holographic interferometry to the measurement of material response has significantly altered and expanded the above picture, and it is the purpose of this letter to report on the first of these experiments. By means of this technique, it is now possible to study the multidimensional response of complex heterogeneous materials to pulsed electron beam dep-

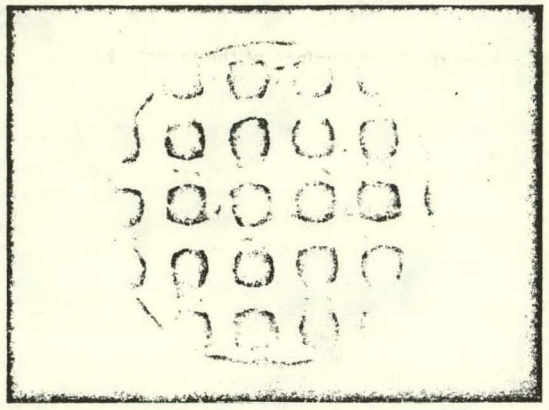

FIG. 1. Cross section of three-dimensional quartz phenolic. The dark spots are radials and the light regions are laterals (see Ref. 5).

FIG. 3. Holographic interferogram of the back surface of an aluminum target.

osition (or for that matter to other stress wave generating techniques). As a consequence of this, it will be possible to learn more about two-dimensional response to finite electron beams as well as shock generation and propagation in complex materials and structures.

The electron beam chosen for the presently reported results was one extracted from a Febetron 705 machine.[4] The beam characteristics were the following: an average energy of 1.5 MeV, a current of 6000 A, and a triangular pulse with a rise time of 20 ns and a base width of 90 ns. The intensity and size of the beam (cal/cm^2) were controlled by a combination of aperturing and an externally pulsed magnetic field. The beam was drifted outside the field emission diode at atmospheric pressure in a chamber where the target was located. Increasing the magnetic field strength had the effect of increasing (focusing) the beam intensity at a given axial position.

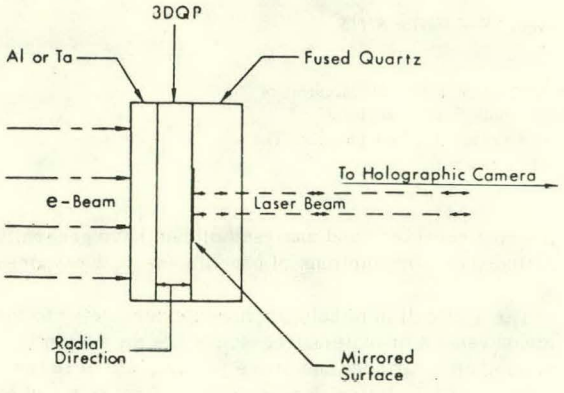

FIG. 2. Holographic photography technique. Target construction in the 3DQP experiments. The overlays of aluminum and tantalum were 0.32 and 0.10 cm thick, respectively; the 3DQP was 0.2 cm thick and the quartz window was 1.27 cm thick. The hologram scene was a 1.27-cm-diam mirrored surface.

Two materials were chosen for the initial study. A disk of aluminum 6061-*T*6 alloy, 5 cm in diameter by 1 cm in thickness, was polished on one face to a mirror finish and employed as a target to demonstrate the feasibility of the technique. The shock generation and propagation characteristics of this alloy are well known. The other material (complex) was orthogonally woven three-dimensional quartz phenolic (3DQP).[5] Characteristics of shock propagation in 3DQP are not at all well known and have been the subject of recent investigations using the more standard methods of plate impact and quartz gauges.[6] The target, in the case of the composite 3DQP, consisted of the specifically constructed laminate structure shown in Fig. 1. An overlay of tantalum or aluminum was used to absorb all the electron energy. Initially, bare 3DQP was employed as the stress-*generation* medium, but because of its very low Grüneisn parameter ($\gamma \sim 0.1$ compared with $\gamma = 1.6$ for tantalum and $\gamma = 2.1$ for aluminum) only a fraction of a fringe was

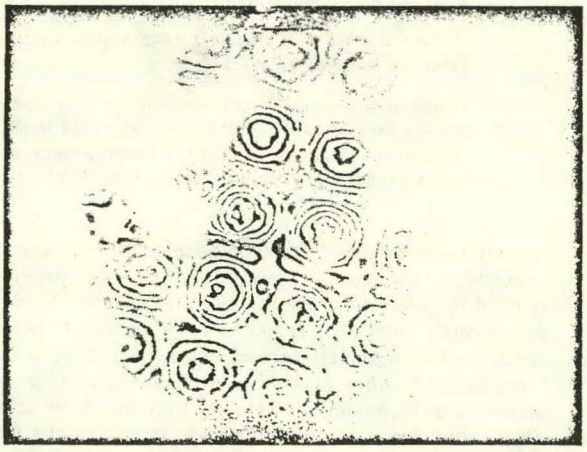

FIG. 4. Holographic interferogram of the mirror surface for three-dimensional quartz phenolic with the tantalum overlay. The time of the second hologram exposure was 0.79 μs after energy deposition.

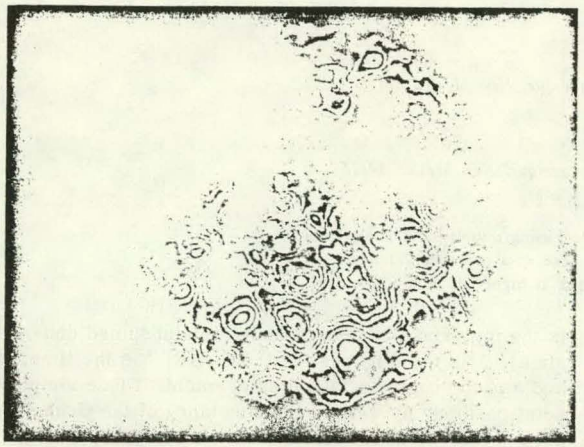

FIG. 5. Holographic interferogram of the mirror surface for three-dimensional quartz phenolic with the aluminum overlay. The time of the second hologram exposure was 1.06 μs after energy deposition.

observed in the holographic system. In this paper, we present only the results for the configuration shown in Fig. 2 where a sufficiently high-stress amplitude was generated by the electron beam so that a rather well-defined response was obtained after *propagation* through 2 mm of 3DQP. On the back of the 3DQP a 1.27-cm thickness of fused quartz was bonded, and between the quartz window and the 3DQP a 1.27-cm diameter mirror (vapor-deposed aluminum) provided the reflecting surface for the hologram scene.

Holographic exposures were accomplished using 3-ns 10-mJ pulses from a PTM ruby laser. The scene beam was expanded and reflected from the mirror surface of the specimen and imaged onto the film. The reference beam was passed through a delay leg and expanded to uniformly illuminate the film. Two holographic exposures were obtained by firing the laser both before and after the arrival of the electron pulse. The second pulse was timed so that the scene was undergoing deflection due to the arrival of the electron-beam-induced stress wave. The interference pattern was then proportional to the surface deflection, each fringe corresponding to a change in position of one-half the ruby wavelength or about 0.35 μm.

In Fig. 3, the holographic interferogram of the back surface (about 2 cm diameter) of aluminum after being exposed to an electron pulse of energy of about 10 cal/cm^2 is shown. The circular fringes indicate that the surface is bowed out by the arrival of the stress wave. The bow shape is a manifestation of the fluence distribution across the front surface of the target. Figures 4 and 5 show the interferograms for the motion of the interface mirrors in the two samples of 3DQP.

In both of the 3DQP cases, the interferograms indicate sets of localized fringes. For the tantalum overlay, the second holographic pulse occurred at 0.79 μs after deposition, and for the aluminum overlay the second pulse occurred at 1.06 μs after deposition. At the earlier time, the localized fringes were centered about the geometric centers of the radials, while at the later time the fringes were localized at the lateral positions. These observations support the hypothesis of a multiple-wave structure for propagation in the 3DQP. The interferograms show that strong relative motion had occurred between the radials and laterals of the material. Because of the hetergeneous character of 3DQP, it is reasonable to expect at least a two-wave structure based on the different sound speeds attributable to the two components. Such an interpretation had been suggested in previous experiments using quartz gauges and ordinary laser interferometer instrumentation. On the other hand, no such multiple-wave structure had been observed in studies[7,8] of the more homogeneous composite 2DQP.

In conclusion, it appears that the holographic technique should have useful applications in the response of complex materials and structures to shock waves and pulsed radiation.

*Work supported by the U.S. Atomic Energy Commission.

[1]F. C. Perry, Appl. Phys. Lett. 17, 478 (1970).
[2]F. C. Perry, J. Appl. Phys. 41, 5017 (1970).
[3]R. A. Graham and R. E. Hutchison, Appl. Phys. Lett. 11, 69 (1967).
[4]Field Emission Corp., McMinnville, Ore.
[5]This material (see Fig. 1), having a density of ~1.80 g/cm^3, is composed of ~75% (by weight) fused-quartz fiber bundles and ~25% phenolic resin. The fiber bundles in the material are of two types: (i) "radial" bundles which run parallel to one another in one direction and "lateral" bundles which run in the two orthogonal directions. The radials have nominally circular cross sections, ~0.06 in. in diameter and are placed in the matrix in a square array on ~0.10-in. centers. The laterals have nominally rectangular cross sections, ~0.01 in. thick by ~0.04 in. wide, and are put down in layers in such a way that in a single layer all laterals run in the same direction and each lateral runs between two adjacent rows of radials. The direction of the laterals alternates in going from one layer to the next. The 3DQP specimens were in the form of circular disks, cut so that the direction of wave propagation was parallel to the radials.
[6]D. E. Munson, Sandia Laboratories Report No. SC-DR-71 0584, 1972 (unpublished).
[7]N. C. Anderholm and R. R. Boade, J. Appl. Phys. 43, 434 (1972).
[8]F. C. Perry, J. Comp. Mater. 6, 2 (1972).

Characterization of the dose from a pulsed electron beam using holographic interferometry*

L. P. Mix

Electron Beam Physics Division 5242, Sandia Laboratories, Albuquerque, New Mexico 87115

F. C. Perry

Applied Material Science Division 5167, Sandia Laboratories, Albuquerque, New Mexico 87115

(Received 2 November 1973; in final form 16 January 1974)

Energy deposition of a pulsed electron beam has been investigated using double-pulse holographic interferometry. The technique has been shown to provide depth-dose data over the illuminated area for a thermoelastic absorber. Possibilities of employing the method at higher doses are discussed.

In a recent paper,[1] we discussed the use of holographic interferometry and intense pulsed electron beams in material response applications. The purpose of this paper is to describe an important additional use of the holographic technique, i.e., an electron-beam diagnostic or dosimetric application.

Previous studies[2–4] with very intense electron beams have shown that laser interferometer measurements of displacement or velocity-time histories along with an analytic solution of the one-dimensional thermoelastic equations can provide quantitative data for the one-dimensional depth-dose profile in an appropriate material. If the target material is homogeneous, behaves elastically, and the Grüneisen parameter is independent of energy, then the deposited energy can be written[2]

$$E(L-at)=(a/\Gamma)u_t(L,t) \tag{1}$$

or

$$E(L-at)-E(L+a\tau_0-at)=(a\tau_0/\Gamma)u_{tt}(L,t). \tag{2}$$

Equation (1) applies to those situations where the energy can reasonably be assumed to be deposited instantaneously, and Eq. (2) must be used when a finite duration τ_0 is assigned to the electron pulse width. E is the energy per unit mass, a is the dilational sound velocity, Γ is the material Grüneisen parameter (assumed constant), L is the thickness of the target, t is the time, and u is the back-surface displacement. These simple relationships, as well as the constancy of the Grüneisen parameter, derive from linear behavior of the thermally stressed material; i.e., the squares and products of strain components and temperature changes are negligibly small compared to the quantities themselves.

Double-pulse holographic interferometry has been applied to the problem of measuring electron dose. The technique involves the double exposure by laser pulses (PTM ruby with ~3 ns duration) reflected from the target surface, once when the target is unstressed—before the electron-beam pulse—and the other when the material is in a stressed condition. The experimental apparatus was the same as that described in Ref. 1. The timing of the second pulse is arbitrarily placed after the electron beam pulse and would normally occur when the electron-beam-induced stress wave is propagating in the target material. The reconstructed scene then shows interference fringes which give the net displacement of the surface at the time of the second exposure.

One can easily see that if the conditions for one-dimensional thermoelasticity are met, then holographic interferograms of pulse-heated targets taken at different

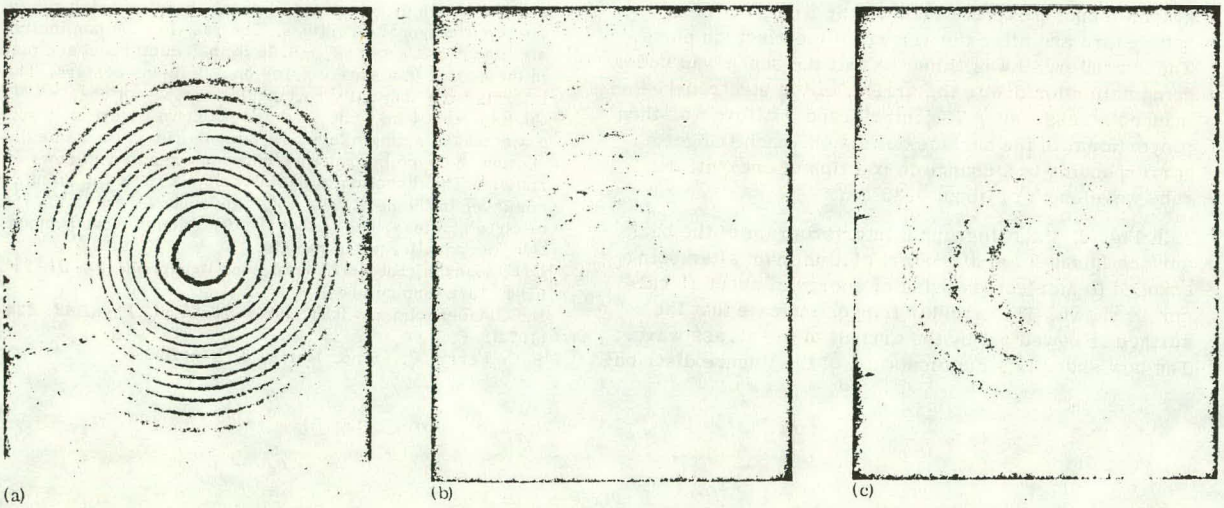

(a) (b) (c)

FIG. 1. Holographic interferograms of the back surface of an aluminum target at discrete times after energy deposition; (a) 0.92 μs, (b) 0.82 μs, and (c) 0.72 μs. An interferogram giving the lowest data point obtained at 0.62 μs is not shown. The scribe markers are set 0.508 cm apart.

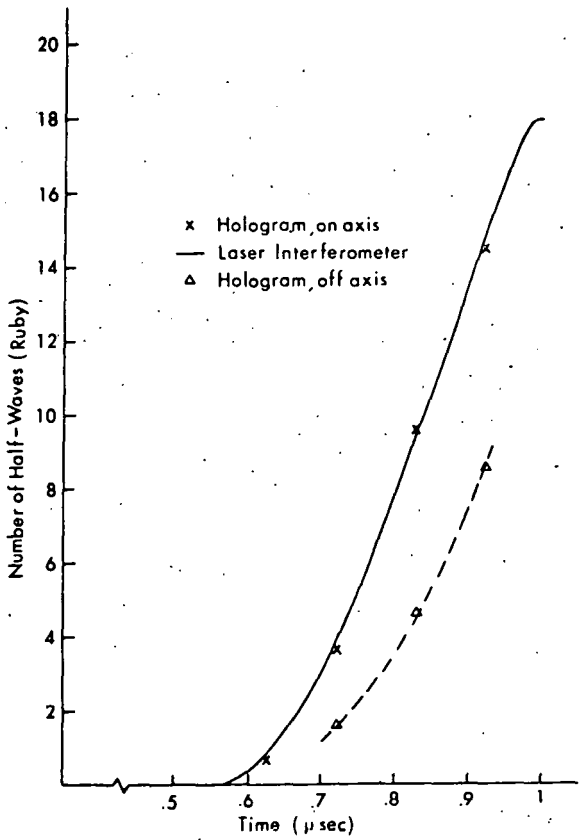

FIG. 2. Comparison of on-axis (×) and 0.3 cm off-axis (Δ) holographic displacements with Michelson interferometer displacement-time history. Each hologram point corresponds to one electron pulse while the interferometer time history was taken on a single shot.

instants of time during the compressive wave cycle should provide response data interpretable in the sense of Eqs. (1) and (2). That is, the displacements obtained holographically at the rear surface for selected times $t \leq L/a$ correspond to the compressive wave displacements obtained by conventional interferometry at those times. The holographic information, in addition, provides displacement data over a large portion of the target surface. The symmetry of the beam, insofar as radial stress wave smearing does not occur in propagation through the target, can be obtained from the surface displacement. In addition, the one-dimensional thermoelastic analysis can be applied to off-axis points to provide off-axis depth-dose profiles.

The technique has been applied to a target of 6061-T6 aluminum exposed to pulses of ~1.5 MeV electrons and 6000 A. The electron pulses (peak fluence or energy flux of about 10 cal/cm^2) were triangular in shape with a 20-ns risetime and 90-ns-base width. The aluminum target was cut in the form of a disk having a thickness of 0.635 cm and diameter of 5.08 cm. Back surface interferograms taken at three instants of time (averaged over the 3-ns-laser pulse) are shown in Fig. 1. These holograms, of course, correspond to three separate electron-beam pulses which have expected reproducibility of ±10%. The times of the second-laser pulses were chosen to lie within the band $L - R/a \leq t \leq L/a$, where R is the approximate range of the electrons in aluminum (~0.7 G/cm^2 or 0.26 cm, where the density is 2.7 G/cm^3).

It can be seen from Fig. 1 that the fringe pattern implies a highly peaked fluence or energy flux (cal/cm^2) distribution, which is a consequence of the upstream aperture and high magnetic focusing field (~4000 G). The centers of the fringe patterns actually lie on the geometric axis of the electron beam, since the scribe lines on the target were not exactly centered. The rear surface area illuminated by the laser corresponds approximately to a 1.7-cm diameter.

In order to determine whether the displacements obtained holographically at discrete times correspond to the displacement-time history resulting from ordinary interferometric measurements, a comparison was made with previous Michelson interferometer records. Figure 2 shows such a comparison where the time history is normalized to the on-axis holographic points. Also shown are the holographic displacements obtained at a point 0.3 cm off the target center. It is seen that the agreement in shape for on-axis response is excellent, thus supporting the contention that the holographic technique can provide a good measurement of off-axis response. These data can then be related to the fluence or energy-flux distribution through the one-dimensional theory. This is demonstrated in Fig. 3. For example,

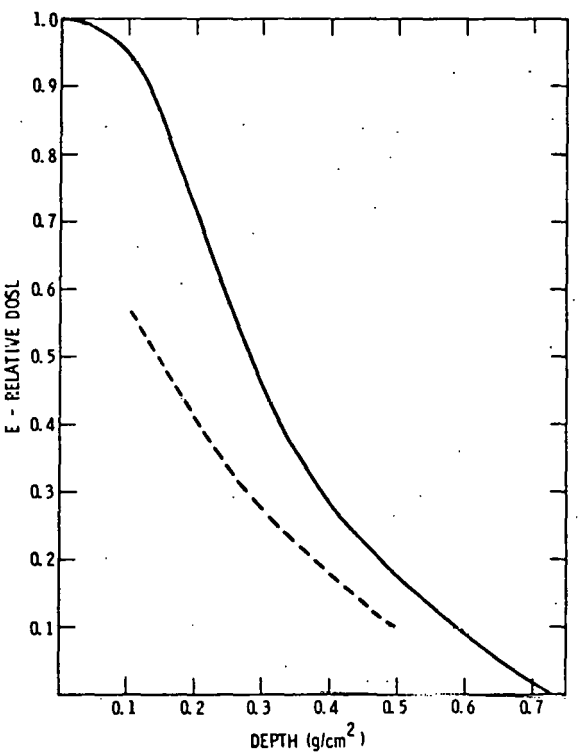

FIG. 3. Comparison of on-axis (solid curve) and 0.3 cm off-axis (dashed curve) depth-dose profiles in aluminum. The profiles were obtained using the curves of Fig. 2 along with Eq. (2). The complete on-axis profile is shown, because the Michelson interferometer record was used for early and late times in the analysis ($t < 0.72$ μs and $t > 0.92$ μs).

in the case studied, the fluence is quite symmetric, and at points 0.3 cm off axis it is down from the peak value by about 70%.

Although the data presented here correspond to rather low electron doses where thermoelasticity is expected to prevail, the technique can be applied to higher doses where plasticity and thermal effects (such as melting and vaporization) would dominate. Under these conditions, the conservation equations couple nonlinearly with the constitutive equation so that a hydrodynamic wave propagation calculation must be employed to relate material response with beam parameters. Limiting factors at high doses are the fringe resolution capability of the holographic film and the speed of the holographic scene. With the present 3-ns laser pulse duration, free-surface velocities are limited to about 10^8 cm/s. However, the use of shorter-pulse-length mode-locked lasers would greatly increase the velocity resolution. It is expected that the holographic technique combined with velocity interferometer data will provide important boundary conditions for the wave propagation analysis of stress waves from tightly pinched electron beams where two-dimensional effects must be included.

*Work supported by the U.S. Atomic Energy Commission.

[1]F. C. Perry and L. P. Mix, Appl. Phys. Lett. 24, 624 (1974).
[2]F. C. Perry, Appl. Phys. Lett. 17, 408 (1970).
[3]D. R. Schallhorn and L. D. Buxton, IEEE Trans. Nucl. Sci. NS-16, 242 (1969).
[4]F. C. Perry and L. D. Buxton, in *Proceedings of the 11th Symposium on Electron, Ion, and Laser Beam Technology* (San Francisco Press, San Francisco, 1971), p. 81.

In-depth heating by an intense relativistic electron beam*

F. C. Perry and M. M. Widner

Sandia Laboratories, Albuquerque, New Mexico 87115
(Received 22 March 1976)

The dynamic response of a planar target irradiated by a tightly pinched intense relativistic electron beam is found to be very sensitive to in-depth heating by the beam due to x-ray deposition and to diode voltage fluctuations. We find that voltage fluctuations are primarily responsible for the observed wave structure preceding the large-amplitude shock wave while x-ray deposition affects the response to a lesser extent. The implications of these results for electron-beam fusion target and accelerator designs are noted.

PACS numbers: 28.50.Re, 45.40.Nx, 52.75.Di, 84.70.+p

The energy deposition profile in a solid target from an intense relativistic electron beam (REB) is an important consideration in the design of targets for inertially confined thermonuclear fusion.[1,2] In particular, it has been shown[3,4] that low-level in-depth heating due to bremsstrahlung x-rays in an ablatively driven implosion can strongly degrade the pusher quality and thus increase the requirements for achieving break-even.

In a recent paper[5] concerning REB energy deposition in solid aluminum targets, we reported that dynamic response data were consistent with classical beam-target coupling. However, an unexplained stress precursor wave, arriving at the back surface before the electron-beam-induced shock wave, could not be deduced from the measured diode voltage and classical deposition. We have considered five possible reasons for the existence of this precursor wave. They are as follows: (i) The equation of state describing stress generation and propagation may be incorrect; (ii) there may be an electron-beam prepulse, although none is observed in electrical measurements; (iii) "hole boring" may occur, i.e., radial motion of material in the deposition volume during the beam pulse which leads to enhanced penetration of electrons; (iv) the x-ray deposition may excite the wave; and (v) there may be some electrons whose energy exceeds the measured diode voltage.

In this paper we present the results of an experiment designed by configuration to obviate the first two mechanisms. The latter three mechanisms must still be considered, although it will be shown that only an additional source of high-energy electrons (but within the error bar of the diode voltage determination) can explain the experimental data. Also, it will be shown that the x-ray deposition is consistent with classical coupling of the beam to the target.

The experimental configuration as well as a data trace are shown in Fig. 1. Instead of a single plate, the anode consists of two aluminum plates in tandem separated by a vacuum gap. The high-amplitude (~1 Mbar) shock is induced in the front plate (facing the Hydra[6] beam) and is decoupled in space and time from the back plate. A velocity interferometer is used to detect rear surface motion of the back plate. The rear surface motion results initially from thermal expansion and a stress wave generated by energy deposition in the back plate and later from the shock arising from impact of the front plate onto the back plate. The areal density of the front plate was chosen to be 0.42 g/cm^2 corresponding to one range (continuous slowing down approximation) for 800-keV electrons.[7] In this configuration only x rays and electrons with energy exceeding 800 keV should be deposited directly in the back plate (areal density 0.86 g/cm^2); therefore, the aluminum will not undergo any phase changes, and only the well-known thermoelastic-plastic behavior for 6061-T6 aluminum[8] must be considered in the analysis. The configuration also eliminates the possible observation of a stress wave arising from beam prepulse, since such a disturbance must arrive at the observation point at a time significantly after the arrival of the impact-generated shock. Hence, any precursor wave to the main shock must be interpreted in terms of mechanisms other than prepulse or equation-of-state considerations.

In Fig. 1(b) a typical fringe pattern is shown with the signal from a PIN x-ray detector on a dual-beam oscilloscope. A noise pulse simultaneous with the x-ray signal (PIN) is followed at approximately 0.4 μs a by well-defined fringe pattern. With the velocity per fringe constant in the experiment of 6.2×10^3 cm/s/fringe, the peak velocity at 0.65 μs is about 1.1×10^4 cm/s. The intensity loss at 0.65 μs corresponds to the arrival at the rear surface of the impact-generated shock wave.

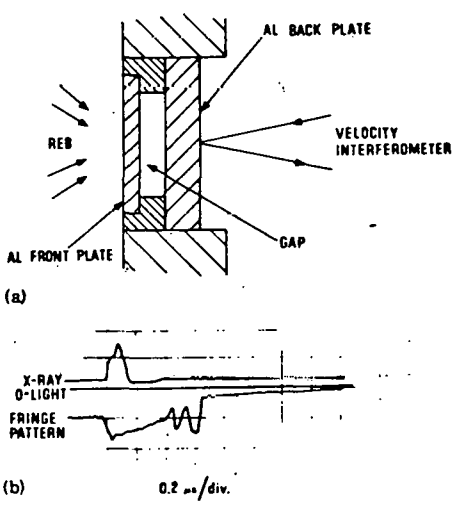

FIG. 1. (a) Diagram of experimental arrangement. (b) Interferometer trace (lower) and PIN detector (upper). The velocity is given by $V=(\lambda/2\tau)N$, where the velocity per fringe constant $\lambda/2\tau=6.0\times10^3$ cm/s fringe.

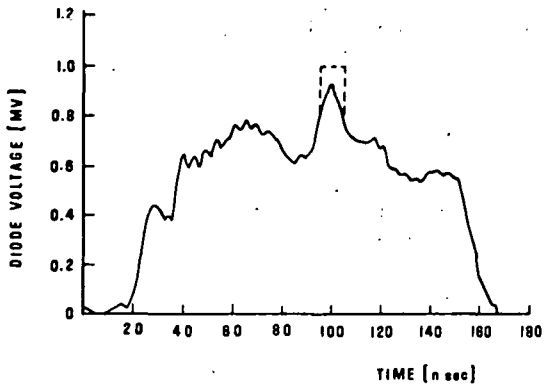

FIG. 2. Corrected diode voltage trace. The solid curve is the unmodified voltage and the dashed curve is the modified voltage.

In this experimental configuration, it is clear that an elastic-plastic wave does precede the shock wave.

In order to explore the effects of "hole boring" and x-ray and electron deposition on dynamic response, we apply the computational procedure in Ref. 5 to the present experiment. This procedure consists of using a two-dimensional hydrodynamic wave propagation calculation[9] with a time- and space-dependent beam pinching model. The electron energy is given by the experimentally measured voltage with a depth-dose profile shape calculated from a one-dimensional transport code[7] for the electron energy 800 keV. The depth of the deposition profile is adjusted as the voltage changes with time.

In Fig. 2 the diode voltage, measured with a capacitive monitor and corrected for the diode inductance, is shown corresponding to the data trace in Fig. 1(b). It is clear that considerable structure exists. A prominent peak at 100 ns arises from a reflection in the transmission line between the diode and switch and is a general characteristic of the Hydra accelerator. A voltage enhancement at that time has been predicted from a circuit analysis of the accelerator.[10] However, both the analysis as well as PIN x-ray measurements suggest that the enhancement is not as sharply peaked as that shown by the voltage monitor.

A comparison of velocity-time histories computed via the above procedure and the experimental profile corresponding to Fig. 1(b) is shown in Fig. 3. The curve denoted as 1 represents the result using the unmodified corrected voltage and the measured 4-mm diameter (FWHM) of the electron-beam pinch. One observes that the position of the sharp shock is in agreement with the experiment, but the amplitude of the precursor wave (arising from deposition by x rays, hole boring electrons, and electrons from voltage deviations above 800 keV) is an order of magnitude lower than the experimental value. By artificially reducing the pinch diameter to 2 mm, we can enhance the effects of hole boring, etc., and the result is denoted as curve 2 in Fig. 3. Again, the calculated wave structure preceding the sharp shock disagrees with the experiment and, in fact, the shock arrival time is in disagreement with experiment.

In order to predict the measured stress wave structure, it is necessary to have greater in-depth heating than would obtain from the measured diode voltage. The desired results (shown as curve 3 of Fig. 3) can be closely approximated by the modified diode voltage in Fig. 2. For this modified voltage we have assumed a square pulse instead of the sharp reflection peak at 100 ns. The pulse magnitude of 1.0 MeV is certainly within the error margin of the voltage measurement and therefore does not represent an anomalous source of electrons. The extreme sensitivity of the dynamic response measurement to voltage fluctuations can be realized by assuming a voltage pulse of 1.1 MeV; the corresponding velocity history is shown as curve 4 (Fig. 3), and the resulting wave structure disagrees with the experimental result.

In order to assess the x-ray deposition, another experiment was performed using a high-Z target (tungsten carbide). The thickness of the target was chosen so that only x rays penetrated through the front plate (0.79 g/cm^2) and were deposited in the back plate (4.73 g/cm^2). The free surface velocity of the back plate was 400 cm/s ±30%. A simple calculation assuming instantaneous deposition and thermoelastic response[11] is appropriate here, so that $v \approx (\gamma/c)E$, where γ is the material Gruniesen parameter (1.4), c is the dilatational wave velocity (0.68×10^6 cm/s), and E is the specific energy absorbed by x rays per unit mass (erg/g). For a total energy deposited during the pinch of about 5 kJ, the absorbed energy per unit mass at the front of the back plate is about 5 cal/g. Thus, the velocity of the

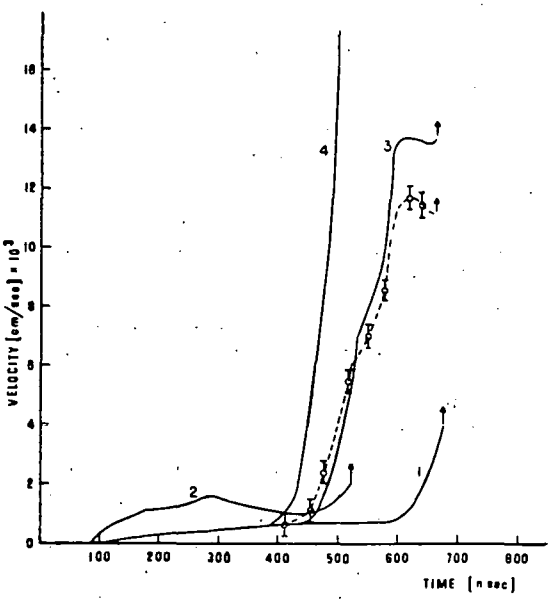

FIG. 3. Calculated velocity time histories and experimental data. Data are represented by circles connected by dashes. Computed histories were obtained using (1) unmodified corrected voltage, 4-mm FWHM pinch; (2) unmodified corrected voltage, 2-mm FWHM pinch; (3) modified corrected voltage, 1.0-MeV square peak, 4-mm FWHM pinch; and (4) modified corrected voltage, 1.1 MeV square peak, 4 mm FWHM pinch, (↑) represents arrival time of sharp shock.

back surface will be about 430 cm/s—in substantial agreement with the experiment.

The implications of these results for REB target and accelerator designs are the following: The beam energy fluctuations described here will give rise to in-depth temperatures several times greater than those which would result only from secondary x rays. Thus, depending on the target design, pusher quality in ablatively driven implosions may be affected. Finally, it should be noted that the voltage enhancement caused by a diode-switch reflection can, in principle, be avoided by employing longer transmission line accelerators. Present concepts for prototype electron-beam fusion accelerators are compatible with this requirement.

The authors thank J.P. VanDevender, Sandia Laboratories, for providing the circuit analysis (SCEPTRE) of the Hydra accelerator and for a careful review of the manuscript.

*Work supported by the U.S. Energy Research and Development Administration.

[1]M.J. Clauser, Phys. Rev. Lett. 34, 570 (1975).
[2]R.C. Kirkpatrick, C.C. Cremer, L.C. Madsen, H.H. Rogers, and R.S. Cooper, Nucl. Fusion 15, 333 (1975).
[3]M.A. Sweeney and M.J. Clauser, Appl. Phys. Lett. 27, 483 (1975).
[4]W.P. Gula and R.C. Kirkpatrick, in Proceedings of the International Topical Conference on Electron Beam Research and Technology, 1975, LA-UR-75-1933 (unpublished).
[5]F.C. Perry and M.M. Widner, J. Appl. Phys. 47, 127 (1976).
[6]T.H. Martin, IEEE Trans. Nucl. Sci. NS-20, 289 (1973).
[7]M.J. Berger, in *Methods of Computational Physics*, Vol. 1, edited by B. Alder, S. Fernbach, and M. Rotenberg (Academic, New York, 1963); J.A. Halbleib, Sr. and W.H. VanDevender, Nucl. Sci. Eng. 57, 94 (1975).
[8]F.C. Perry, Appl. Phys. Lett. 17, 478 (1970).
[9]S.L. Thompson, Sandia Laboratories Report, SAND-74 0122, 1974 (unpublished).
[10]H.W. Mathers, SCEPTRE (System for Circuit Evaluation and Prediction of Transient Radiation Effects), *Network Computer Analysis*, edited by George W. Zoorist (Boston Technical Publishers, Cambridge, Mass., 1969), pp. 169—196.
[11]F.C. Perry, J. Appl. Phys. 41, 5017 (1970).

Energy deposition of superpinched relativistic electron beams in aluminum targets*

F. C. Perry and M. M. Widner

Sandia Laboratories, Albuquerque, New Mexico 87115
(Received 20 January 1975; in final form 2 September 1975)

Dynamic response data, which traditionally have been used to obtain equation-of-state (EOS) information of materials, were instead used here to study energy deposition of an intense ($\sim 10^{11}$ W/cm^2) tightly focused relativistic electron beam (REB). Measurements of the REB-induced shock-wave transit time and average rear-surface velocity were compared with two-dimensional hydrodynamic calculations which contain well-known EOS information for 6061-T6 aluminum. The experimental results were consistent with classical electron deposition, i.e., a one-dimensional Monte Carlo transport calculation. In addition, peak pressures in the range 1–2 Mbar (0.1–0.2 TPa) were implied. Two anomalous effects were observed: (i) a low-amplitude (free-surface velocity $\sim 10^4$ cm/sec) precursor signal, preceding the REB-induced shock wave and (ii) a velocity distribution of material behind the rear surface of the target following the arrival of the REB-induced shock wave.

PACS numbers: 28.50.R, 62.50., 79.20.K

I. INTRODUCTION

The advent of relativistic electron-beam (REB) accelerators with pulsed current outputs in the range 10^6 A/cm^2 has stimulated considerable interest in these machines as a means to initiate controlled thermonuclear reactions.[1,2] Recently,[3] work has concentrated on pinching or focusing these electron beams within small areas (a few square millimeters) in pulses of tens of nanoseconds duration. Under these circumstances sizeable craters are formed in solid metal anodes. It has been suggested[4] that the beam self-magnetic field may affect the classical energy loss and scattering of electrons in the target blowoff in such a way as to enhance the deposition in the blowoff. Also, it has been proposed[2,5] (without experimental evidence) that enhanced electron-beam–target coupling may arise from beam-plasma instabilities. Therefore, the purpose of the present study was to assess the validity of classical energy deposition in the target material using the Hydra accelerator[6] and to determine the extent to which dynamic response data can be useful in establishing the energy deposition profile.

Using the electron-beam parameters from the Hydra accelerator, nominally a 600-keV 350-kA 100-nsec beam, Widner and Thompson[7] have compared cratering in thick aluminum and copper anode plates with predictions of a two-dimensional energy-flow hydrodynamic code called CSQ.[8] To obtain computational damage patterns which agreed with experiment, the computation predicted pressures in the megabar region and peak electron energy depositions of about 10^{12} erg/g. Direct material vaporization by the beam, shock heating, plastic deformation, and spall contributed to the observed damage.

In this paper we will present results of an experimental investigation of the dynamic response of the rear surface of aluminum plates, thicker than an electron range, to the Hydra beam. Traditionally, such data have been useful in characterizing the material equation of state (EOS). However, because of the well-known EOS data for aluminum[8] (in this case 6061-T6 Al), our purpose is to utilize these data with hydrodynamic calculations to obtain information about the deposition of beam energy in the target. The various experimental shock-wave measurement techniques included Velocity Interferometer System for Any Reflector (VISAR),[9] standard interferometry,[10] target reflectivity changes, flash gaps, and beam-splitter–mirror techniques. The response data as well as supplementary diagnostic information were analyzed to characterize the thermodynamic state of the electron-beam-heated and shock-compressed material.

To accomplish the goals the following approach was taken. Diode voltage, current, and x-ray pinhole data were obtained on a shot-to-shot basis and used along with an experimentally determined form for the pinching beam in the hydrodynamic calculations. The form for the time- and space-dependent current density profile was provided by previous investigations of the Hydra electron beam involving time-resolved x-ray pinhole[11] and PIN detector array[12] techniques. The calculations included (i) collisional electron deposition profiles from a one-dimensional Monte Carlo electron transport code similar to that developed by Berger and Seltzer[13] and (ii) a two-dimensional three-phase hydrodynamic code developed by Thompson.[8] Experimental dynamic response data were compared with results of the hydrodynamic calculations.

II. MACHINE CHARACTERISTICS AND EXPERIMENTAL DETAILS

Characteristics of the Hydra accelerator have been previously reported. For this study a single line was used with the nominal electron-beam parameters 650 keV, 360 kA, and 100 nsec. The cathode geometry[14] consisted of a 1-cm-diam cylindrical shell protruding about 0.1 cm from the center of the face of a 12.7-cm-diam brass plate. This cathode has been shown to produce reasonably pinched beams.[11,12] The anode configuration underwent a few minor modifications during the course of the present investigation, and the corresponding changes in diode inductance were incorporated into the analysis of voltage and current records.

The ideal experiment involving the response of solid material to electron-beam heating would be the determination of the continuous velocity-time history of every

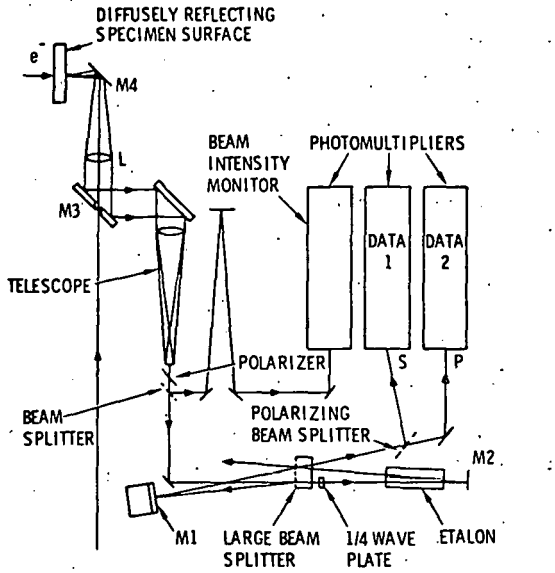

FIG. 1. Velocity interferometer system for any reflector.

point of the rear surface (or interior surface) of the solid from the moment energy begins to be absorbed. In order to measure dynamic response we have employed present-day shock-wave techniques which have been primarily used in previous studies of material properties. Most of the following methods will involve the measurement of dynamic response over the area of a focused laser beam (diameter ~0.1 mm).

Initially, VISAR instrumentation was applied in the dynamic response measurements. When a diffuse specimen surface is used, the instrument is quite insensitive to specimen tilt during the experiment. In this technique, specimen surface velocity u is related to the fringe count F at time t through the relation

$$u(t-\tfrac{1}{2}\tau)=\frac{\lambda_0 F(t)}{2\tau(1+\Delta\nu/\nu_0)}\left(\frac{1}{1+\delta}\right),$$

where

$$\delta=-\frac{1}{n-(1/n)}\left(\frac{dn}{d\ln\lambda}\right)_{\lambda_0}.$$

Here, τ is the initial delay time of the interferometer, λ_0 is the wavelength of light used (514.5 nm), and $\Delta\nu/\nu_0$ is an index-of-refraction correction factor which is equal to zero unless a "window" material is placed on the specimen's reflective surface. The factor δ results from the change in refractive index n in the etalons of the interferometer as the wavelength changes from its initial value λ_0, due to the Doppler shift ($\delta=0.034$ in these experiments).

Figure 1 shows a diagram of the VISAR arrangement used in the Hydra experiments. The photomultiplier tubes and the oscilloscopes had to be placed inside a copper-shielded rf enclosure. Also, the laser interferometer unit was positioned outside a concrete-walled radiation cell, and the argon-ion laser beam was directed through a hole in the wall before focusing on the anode plate. The interferometer has the feature that fringe patterns are recorded in quadrature, i.e., there are two fringe outputs which are 90° out of phase with each other. The benefits of 90°-out-of-phase signals are (i) acceleration can be distinguished from deceleration and (ii) over-all resolution is improved because at all times there will be a fringe record which is not near a maximum or minimum light level. Since intensity changes may be caused by shock-induced changes in surface reflectivity, each fringe signal is recorded along with its intensity on dual-beam oscilloscopes so that suitable corrections can be applied.

In Fig. 2 are shown the output traces corresponding to one of the fringe patterns and intensity. One notes the x-ray-induced noise pulse in both the data and intensity traces followed by about three-quarters of a fringe in the data trace. During the initial fringe record, the intensity remains essentially constant. Following the initial fringe pattern both signals rapidly decrease with increasing time. The interpretation of these traces corresponds to the velocity-time profile also shown in Fig. 2. It is seen that a precursor signal follows the beginning of the x-ray pulse by about 0.2 μs, and the arrival of the shock wave occurs when the intensities start to decrease 0.1 μs later. The peak velocity of the surface could not be determined unambiguously because the fringe contrast approached zero after shock arrival. Also, it appears that after shock arrival at the free surface the fringe contrast began to fluctuate. In principle, it is possible by suitable analysis[15] of the intensity and quadrature traces to distinguish between noise and fringes given the condition that both the contrast and intensity undergo rapid changes. This has been done by the method of Asay and Barker, and the results suggest that the reflected light did not have a well-

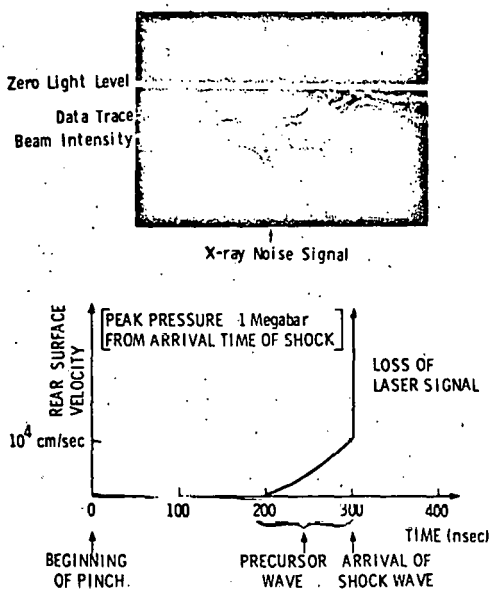

FIG. 2. VISAR oscillograph traces for shot 1245 and free-surface velocity profile—aluminum target (3.05 mm thick). The top trace indicates 0.2-μs time marks, the middle trace is fringe output, and the lower trace is intensity.

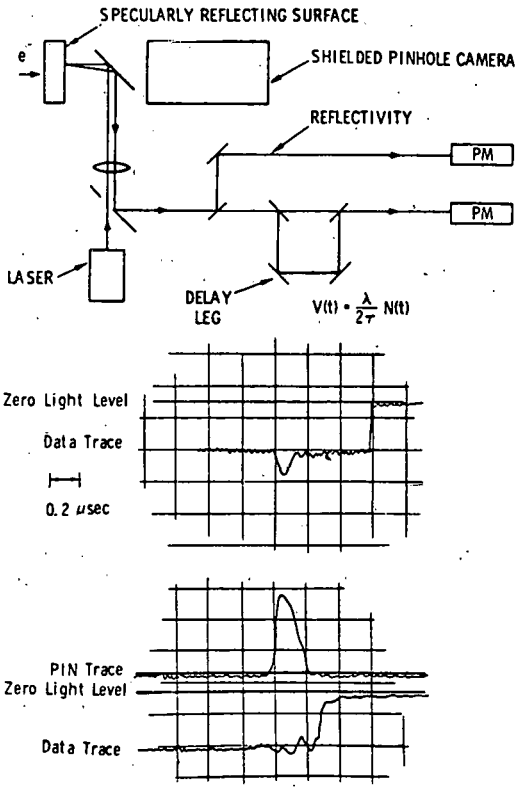

FIG. 3. Experimental arrangement for reflectivity and standard velocity interferometer measurements. The equation relates free-surface velocity V, wavelength λ (632.8 mm), delay time τ, and N the number of fringes observed up to time t. Also shown are typical oscillograms. The top oscillogram (0.2 μs/cm) shows a PIN detector output superimposed on a reflectivity determination of shock arrival, and the lower oscillogram (0.1 μs/cm) indicates PIN output and velocity interferometer data on separate traces. X-ray pinhole photographs are obtained simultaneously with the experiment.

defined Doppler shift. A possible implication is that a distribution of particle velocities exists near the surface after arrival of the shock wave. However, neither the existence of a precursor wave nor the velocity distribution accompanied by a drastic intensity reduction are well understood at this time.

Since the experiment employing the VISAR instrumentation appeared to raise some questions, and we were not able to determine a peak free-surface velocity, it was decided to carry out further experimentation using simpler techniques. One of these methods was simply to record the onset of the reflectivity change associated with the arrival of the shock at the rear surface. Since at the expected high shock amplitudes the pressure is a strong function of the shock speed, the determination of a shock transit time in the target plate should be useful diagnostic information. This is especially true for thin plates (approximately one electron range thick) where the shock has not appreciably diverged. Also, it was decided to attempt ordinary velocity interferometry using specularly reflecting surfaces. This technique should, in principle, be capable of determining the profile of the relatively low-velocity precursor, although it was expected, because of tilt and/or reflectivity change, that no information other than shock transit time would be obtained after arrival of the shock wave.

In Fig. 3 are shown the optical arrangements for both reflectivity and velocity interferometer determinations. In contrast to the VISAR experiment, the back surface of the anode was polished to a mirror finish. Also shown are data traces for each measurement. In the top trace (reflectivity) the output of a PIN x-ray detector was summed with that of the photomultiplier. In this measurement the anode was an aluminum disk with thickness of 0.635 cm. The rapid decrease in intensity at 0.70 μs (shown uncorrected for PIN detector cable length) from the start of the PIN output is interpreted to correspond with the arrival of the shock wave at the free surface. In the lower trace (velocity interferometer) a thinner (~1 electron range) anode was used, and the PIN output was recorded on one sweep of a dual-beam scope. It appears that one to two fringes were recorded prior to the shock arrival at the free surface. This is supporting evidence for a precursor wave which was inferred from the VISAR data. The shock arrival time of about 0.12 μs is in agreement with reflectivity determinations using the thinner plates and comparable electron-beam conditions.

The flash-gap technique[16] was employed to obtain dynamic response data. The anode configuration, shown in Fig. 4, consists of an aluminum plate followed by a thin gap filled with air (1 atm) and covered with a transparent block of Plexiglas. When the electron-beam-

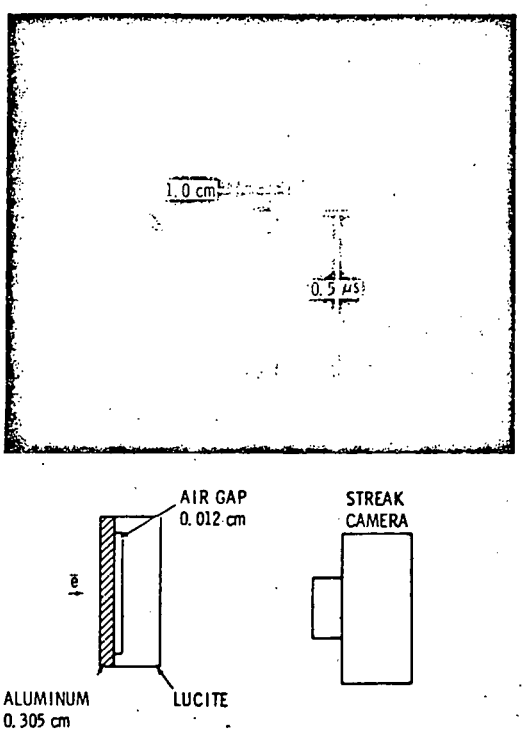

FIG. 4. Target configuration for the flash-gap technique and typical streak photograph.

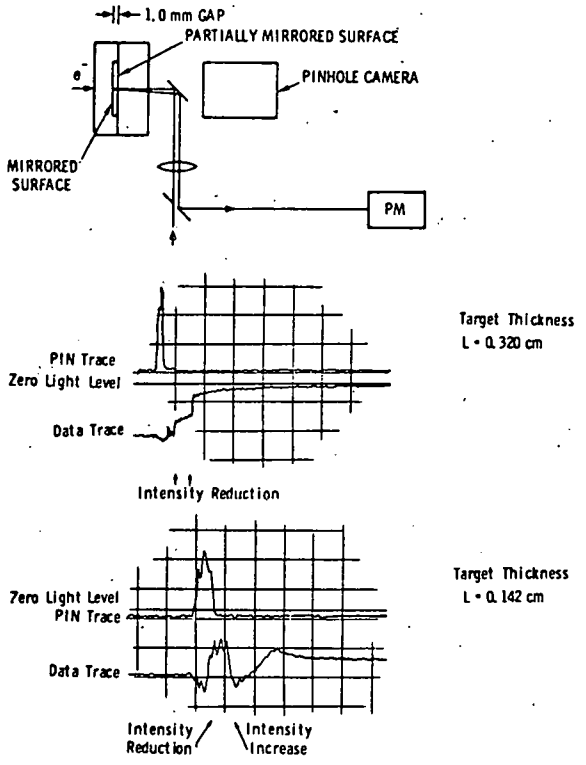

FIG. 5. Diagram of the mirror—beam-splitter method for simultaneous determination of shock transit time and free-surface velocity. Laser intensity modulation and PIN outputs are shown for two target thicknesses (top trace 0.5 μs/cm, lower trace 0.2 μs/cm). A value of 65 ns must be added to the transit times taken from the oscillographs to account for the difference between the light path and the PIN detector cable length.

generated shock wave reaches the rear surface of the aluminum plate, it accelerates this surface and closes the gap between the plate and the plastic block. The air in the gap is heated and compressed by the successive gas shock reverberations and becomes luminous for a short time before heating of the plastic or gap closure effectively shuts off the light. This light is recorded by a fast streak camera. The brightness depends upon the strength of the shock and the gas filling the gap. Argon or xenon are brighter than air, but the air was found suitable in the present study as is shown in the accompanying streak photograph. The photograph also shows the x-ray-induced luminosity of either the plastic block or the phosphor of the streak camera which provides a convenient time fiducial in the experiment. Note also, the structure of the x-ray-induced luminosity; this qualitative intensity variation has been shown to occur in the response of PIN detectors.

Previous investigation of shock waves using flash gaps have always been concerned with planar shocks. It is quite obvious from the streak photograph of Fig. 4 that we do not have a plane shock as we would expect from the dimensions (a few millimeters) of the electron beam. In fact, it appears that the radial velocity of the luminous front changed gradually from the moment of shock arrival out to a time when the slope is relatively constant. This is interpreted as the velocity of the shock wave traveling in air perpendicular to the beam axis. We can use this interesting observation to infer something about the free-surface velocity of the aluminum plate.

From the gas dynamics of strong shock waves we know that the velocity of the "piston" (rear surface) creating the wave is given by[17]

$$u=\frac{2}{1+\gamma}D,$$

where D is the shock velocity in the gas and γ is the ratio of specific heats. In the photograph of Fig. 4, the shock velocity is about 10 times the ambient sound speed. The value of the free-surface velocity is, therefore, approximately 3×10^5 cm/s. One can also estimate the free-surface velocity from the time of shock arrival to the time the light shuts off on the center of the streak. In the present case, the value is almost an order of magnitude lower than the above estimate of 3×10^5 cm/s. Such a low value, representing a lower bound for the free-surface velocity, is in error because of the severe nonplanarity of the shock and the unknown duration of the luminescence after impact. That is, heating of the plastic or gap closure may not immediately shut off the light to the camera.

The final dynamic response technique used is called the beam—splitter-mirror method which was designed to make simultaneous determinations of shock transit time and free-surface velocity. In Fig. 5 is shown the specially fabricated target anode and associated optics. The method consists of collinearly reflecting a laser beam partly from a beam splitter and partly from the mirrorized surface of an aluminum anode—the two are separated in vacuum by a specified distance (~1 mm)—and measuring the changes in reflected light intensity with a photomultiplier-tube oscilloscope. The arrival of the shock at the aluminum rear surface is accompanied by an abrupt decrease in intensity, and the impact of the free aluminum surface on the surface of the splitter causes another intensity change. From the dimensions of the anode-splitter assembly and the record of light intensity changes, it is possible to infer free-surface velocity spatially averaged over the gap.

The oscillographs shown in Fig. 5 are examples of data traces for this technique. Again the output of a PIN detector is indicated on the top trace of each record. For the 0.32-cm-thick plate some noise on the PM output is followed by a sharp reduction in light intensity at 0.3 μs (from the start of the PIN output, but uncorrected for PIN detector cable length) corresponding to the shock arrival at the rear surface of the plate. At a time 0.3 μs later the light intensity is further reduced; the intensity drop here is attributed to the destruction of the dielectric coating of the beam splitter by impact of the aluminum. The free-surface velocity averaged over the interval is 0.3 cm/μs. For the thinner 0.142-cm aluminum plate the behavior is quite different. The shock is presumed to arrive at the free surface at a time of approximately 0.1 μs (uncorrected) after the start of the PIN signal. This time corresponds to a reduction in intensity as expected. However, the

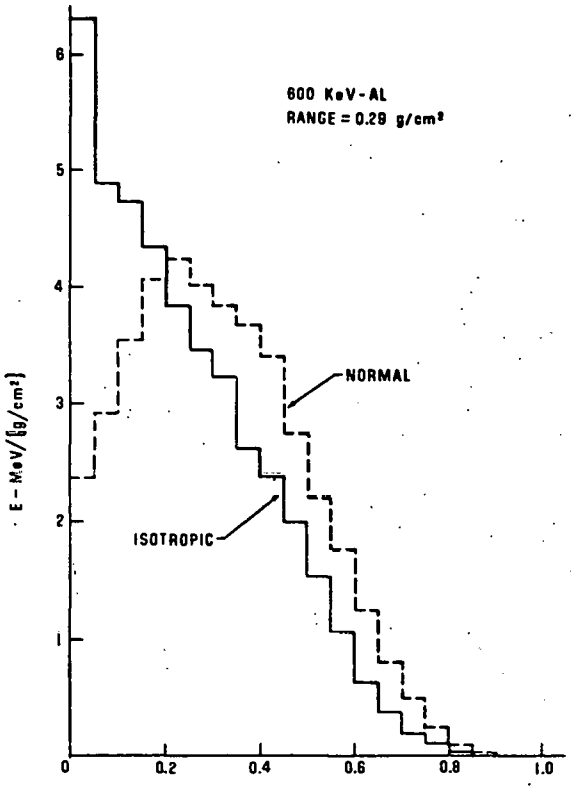

FIG. 6. Deposition profiles (normal and isotropic electron angular distributions) for 600-keV electrons.

next break in intensity occurs at about 0.26 μs and corresponds to an increase in intensity followed by a slower decrease and leveling off. This increase in intensity is attributed to the self-luminosity of the quartz beam splitter due to the impact of a sufficiently high-velocity aluminum flyer plate. The duration of the self-luminosity results from the nonplanarity of the shock and the quenching in the quartz. According to this interpretation the free-surface velocity is approximately 0.7 cm/μs.

III. COMPUTATIONAL MODEL AND COMPARISONS

The dynamic material response was calculated using a two-dimensional hydrodynamic code CSQ which contains a three-phase equation of state. Saha equilibrium is assumed for ionization and material properties are employed in elastic-plastic and fracture calculations. For these calculations the shock transit time in the material is comparable to the duration of the electron-beam pulse; therefore, attention was given to the time and spatial modeling of the electron beam. The current density profile used in the calculations is based upon experimental time-resolved pinhole[11] and PIN detector array studies.[12] For detailed comparisons with the results of particular shots we employed the experimentally obtained voltage and current traces with the following current density profile

$$J(r) = J_0(1 - r/r_b), \quad r < r_b$$
$$= 0, \quad r \geq r_b,$$

where r_b is the beam radius and J_0 is the current density on axis ($J_0 = 3I/\pi r_b^2$, where I is the total current).

The time-dependent beam collapse is modeled using

$$r_b = r_{b0} - V_p t, \quad r_{b0} - V_p t > r_p$$
$$= r_p, \quad r_{b0} - V_p t \leq r_p,$$

where r_{b0} is the initial beam radius (chosen to be the cathode radius = 6.35 cm), V_p is the pinch collapse velocity = 10^8 cm/s, and r_p is the final pinch radius. The value of r_p is taken to be the full width at half-maximum of the x-ray pinhole trace for each electron-beam shot. In this form for $J(r)$ 50% of the current is contained in the full width at half-maximum, which is consistent with the PIN array measurements.

The electron energy is given by the experimentally measured voltage with a depth-dose profile shape calculated by a one-dimensional Monte Carlo electron transport code for the electron energy 600 keV. The electron penetration is varied with voltage using a single shape for the depth-dose profile. One might object to using a single profile shape valid for an energy of 600 keV, since it does not correctly model the profile shape and larger specific energy absorption for low-energy electrons. However, it is argued that low-energy electrons are present primarily in the early portion of the beam pulse where significant pinching has not yet occurred. Also, we will demonstrate later in a sensitivity analysis the effect on the results of decreasing the effective electron range and increasing the energy absorbed per unit mass near the front of the target.

The exact angular distribution of electrons impinging on a solid anode is not known. For the purpose of comparison with experimental results both normal and isotropic angular distributions were assumed in the electron transport calculations. In Fig. 6 are shown the deposition profiles using these angular distributions for 600-keV electrons in aluminum. Not shown, because of the linear scale, are the low-level x-ray tails. Both of these profiles will be used in comparisons with data.

We compare in Fig. 7 the results of calculations with experimental shock transit time and free-surface velocity (measured by the mirror—beam-splitter method). This figure shows the calculated shock and free-surface trajectories for both the normal and isotropic distributions. The "off-axis" shock and surface trajectories are shown because the experiments generally yielded crater or hole positions which were not centered on the geometric axis of the diode. We were not able to use the pinhole camera results to accurately locate the position of the electron-beam pinch in the anode plane. The pinch location relative to the geometric axis of the diode (and, therefore, the focus of our laser beam) had to be estimated after each shot from the position of the hole produced by the pinched beam. The error in these estimations arose from the irregular boundaries of these holes, i.e., their centers were not exactly defined. For example, in shots 2052 and 2060 (Fig. 7) the off-center positions were each estimated to be 2 ± 0.5 mm. However, accounting for these errors, it is seen from Fig. 7 that the calculational model is quite successful in predicting the experimentally measured shock transit and rear-surface position. Also, one observes that the shock and surface trajectories are almost the same for the normal and isotropic angular distributions,

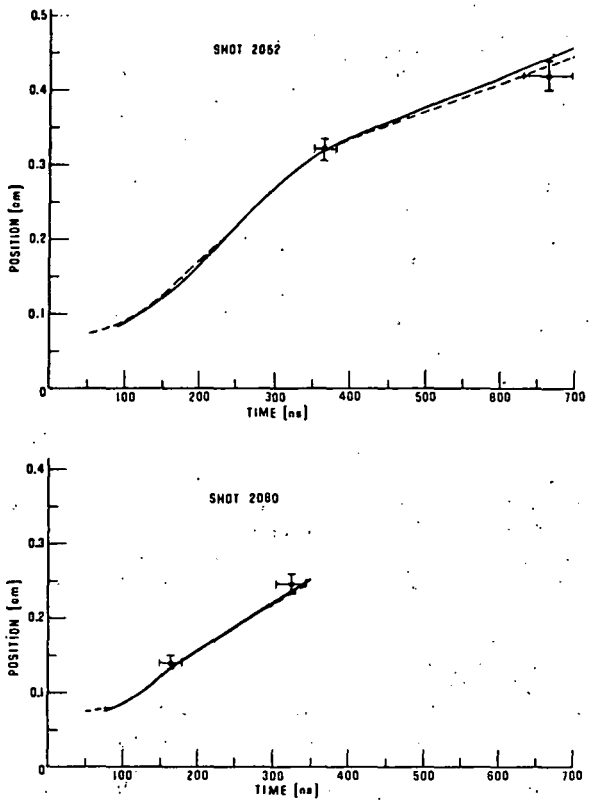

FIG. 7. Comparison of experimental dynamic response using the mirror—beam-splitter method with calculated shock and free-surface trajectories for (a) shot 2052 and (b) shot 2060. Solid and dashed trajectories correspond to isotropic and normal angular distributions, respectively.

and the experiment is not capable of distinguishing between them.

All of the data are summarized in Table I where we have included both the calculated "on-axis" and "off-axis" results. Except where indicated in Table I the model calculations were based on a normal angular distribution of electrons. In cases where only the shock transit times were measured, the model predictions are in reasonable agreement with the experimental values. In shot 1515, the large difference between predicted and measured transit time may be attributed to the particularly large uncertainty in crater position for that case. That is, for a "thin" anode the damage caused by 13 kJ of beam energy precludes an accurate estimate of the beam position. In general, however, the discrepancies between experimental values and model predictions lie within 10%.

In order to examine more carefully the effect of the deposition upon dynamic response, we have made additional hydrodynamic calculations. The input conditions and the results of the calculations for shot 2060 are shown along with the experimental data in Table II. An isotropic distribution of incident electrons, corresponding to footnote c of Table I, was used to calculate the deposition profile. This was selected as the reference case and three additional variants of this profile were examined. These variants consisted of (i) reducing the total energy by one-half, (ii) reducing the penetration depth by one-third, and (iii) simultaneously reducing the penetration depth by one-third and reducing the pinch radius r_p by one-half. It is seen that either reducing the energy *or* the penetration depth decreases the rear-surface velocity despite the fact that the energy absorbed per unit mass in the latter case was significantly higher. By comparing the calculated off-axis portions in Table II with the data of Fig. 7, one observes that the calculated results for all three deposition variants lie outside of the error bars of the experiment.

Because two-dimensional hydrodynamic calculations are quite expensive in terms of computer time, we were not able to make these sensitivity comparisons for all electron-beam shots. Instead, we have concentrated our efforts on shot 2060. This shot was most appropriate because it involved a thin aluminum target where the effects of shock divergence will be minimized. An isotropic distribution of incident electrons was assumed for the standard case since it is generally believed that electrons with incident angles other than

TABLE I. Data summary.

Shot No.	Target thickness (mm)	Total beam energy (kJ)	Beam pulse duration (ns)	X-ray pinhole r_p (mm)	Crater position off axis (mm)	Shock transit time (ns)			Time to beam splitter (ns)			Free-surface velocity[b] (10^5 cm/s)	Free-surface velocity[b] (10^5 cm/s)		Peak pressure (Mbar)
						Expt.[a]	Model		Expt.	Model		Expt.	Model		
							On axis	Off axis		On axis	Off axis		On axis	Off axis	
1245	3.05	7.2	120	6.0	0.0	300	300	...	...	...	...	...	4.1	...	1.47
1515	1.60	12.7	146	4.0	5.0	180	150	225	...	...	...	...	8.8	...	2.13
1517	3.05	13.0	146	5.0	5.0	385	305	370	...	...	...	...	5.8	...	1.64
1518	6.35	12.2	146	3.0	3.5	765	640	740	...	...	...	...	2.7	...	2.34
2052	3.20	8.1	194	4.0	2.0	365	355	365	665	545	630	3.3	5.2	3.7	1.25
2052[c]	3.20	8.1	194	4.0	2.0	365	350	370	665	560	605	3.3	4.7	4.2	1.33
2060	1.42	7.9	166	4.0	2.0	165	170	170	325	300	345	6.5	8.0	5.9	1.25
2060[c]	1.42	7.9	166	4.0	2.0	165	155	175	325	295	335	6.5	7.4	6.5	1.36

[a]Times here have been corrected for a 65-ns time difference between the light path and the PIN cable.
[b]Velcoities based on gap widths of 0.99 and 1.04 mm for shots 2052 and 2060, respectively.
[c]Model calculation based on an isotropic electron angular distribution.

TABLE II. Comparison of special cases with experiment (Shot 2060).

Deposition assumption	Shock transit time (ns)		Time to beam splitter (ns)		Free-surface velocity (10^5 cm/s)	
	On axis	Off axis	On axis	Off axis	On axis	Off axis
Experiment		165		325		6.5
Isotropic (normalized) Monte Carlo	155	175	295	335	7.4	6.5
Isotropic (normalized) energy reduced by one-half	175	180	350	400	5.9	3.6
Isotropic (normalized) electron depth of penetration reduced by one-third	200	200	395	485	5.3	3.6
Isotropic (normalized) depth of penetration reduced by one-third and pinch radius r_p reduced by one-half	160	205	275	395	9.0	5.5

normal must constitute a major fraction of the pinched beam. We expect that the above deposition profile variants will cause changes in the dynamic response of thicker targets, e.g., shot 2052. We know, for example, that the physical reason for a lower surface velocity (increased time to beam splitter in these experiments) for the case of a profile with reduced penetration depth is simply an enhanced pressure relief during the deposition time. On the other hand, the experiment will be less sensitive to such variants for long shock running times as in thicker targets. It is reasonable to restrict our rather expensive computer calculations to a single well-characterized experimental shot where the sensitivity to variations in the deposition profile is maximized. For this reason we again concentrate on shot 2060 in the following analysis.

As a further demonstration of the relationship between "range-shortened" deposition profiles and the experimental results, we show in Fig. 8 the shock and free-surface arrival times calculated for the conditions of shot 2060 with a deposition profile whose range is arbitrarily foreshortened. The calculated results are indicated by bands; and the width of these bands were determined by the uncertainty of ± 0.5 mm in the beam pinch position at the anode face. The experimental bandwidths just reflect the intrinsic uncertainty of the response measurements. We see that the surface "flight" time is quite sensitive to the range-shortened profile and the shock transit time is less sensitive. From the comparisons shown in Fig. 8 we can say (i) the experiment is consistent with the classical deposition profile with $r_a/r_0 \gtrsim 0.85$ and (ii) the best agreement occurs for $r_a/r_0 = 1$, i.e., the classical range.

Finally, it is important to note that an attempt was made to explain the experimentally observed precursor wave by inclusion of the x-ray deposition tail (calculated by Monte Carlo transport) in the hydrodynamic computation. The calculated rear-surface velocity resulting from thermal expansion was approximately an order of magnitude below the measured amplitude.

IV. SUMMARY AND CONCLUSIONS

We have applied various shock-wave techniques including laser interferometry to the investigation of dynamic response of solid anode targets to a superpinched electron beam. These methods were successful in determining free-surface velocity profiles, shock transit times, and average free-surface velocities of aluminum targets. The time and spatial dependence of the beam current density was combined with collisional electron energy deposition and used in a two-dimensional hydrodynamic calculation of dynamic response. In the experiments thin (1.5 times the electron range) as well as thicker targets were employed, since the dependence of dynamic response on beam size and energy is strongest for thin targets where shock divergence is smaller.

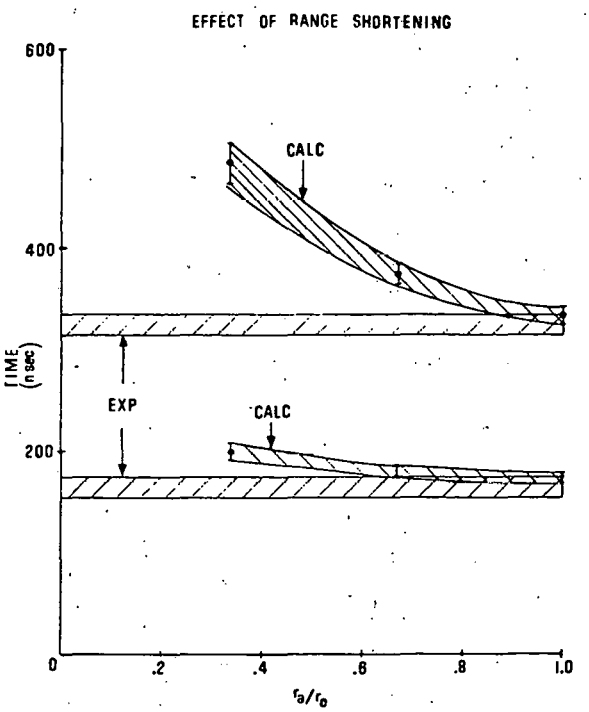

FIG. 8. Effect of decreasing deposition range on shock transit and rear-surface arrival times for shot 2060. Horizontal bands represent experimental values and the curved bands are the calculated result.

Comparison of experimental results with model predictions on a "shot-by-shot" basis indicated reasonable agreement. Peak free-surface velocities (measured) were about 7×10^5 cm/s, and peak pressure varied from about 1 to 2 Mbar near the deposition region. Both normal and isotropic angular distributions were used in depth-dose computations, although the experiments were not sufficiently accurate to distinguish between the two distributions. In general, it appears that these shock-wave data are consistent with classical coupling (electron transport) between the electron beam and the target even at these very high current densities. We do not unequivocally rule out anomalous deposition mechanisms. However, we have shown that the dynamic response is sensitive to the form of the deposition profile, and response data can provide an important test for the validity of transport calculations.

There were two observations of anomalous behavior. One was the interferometric observation of a precursor signal which was not predicted by the computation. The energy associated with this wave corresponds to only a few percent of the total absorbed energy. Such a disturbance might arise from a long tail on the energy deposition profile; however, it was shown that the tail associated with x-ray production in the one-dimensional transport calculation was insufficient to account for the experimental result.

Another phenomenon observed in interferometer experiments was the probable existence of a velocity distribution near the rear surface of the target upon arrival of the shock wave. The loss in light intensity and fringe contrast when the shock arrived at the rear surface supports this conclusion.

ACKNOWLEDGMENTS

The authors express special thanks to D.W. Dugan for his expertise throughout all of the experiments. Technical support with the VISAR instrumentation and many discussions were appreciated with J.R. Asay, B.M. Butcher, L.A. Kent, and C.L. Witten. Many helpful discussions were held with M.J. Clauser, A.J. Toepfer, S.L. Thompson, and G.Yonas for which the authors are grateful.

*Work supported by the U.S. Energy Research and Development Administration, ERDA.

[1]G. Yonas, J.W. Poukey, J.R. Freeman, K.R. Prestwich, A.J. Toepfer, M.J. Clauser, and E.H. Beckner, *Proceedings of the 6th European Conference on Controlled Fusion and Plasma Physics* (U.S.S.R. Academy of Sciences, Moscow, 1973), p. 483.

[2]L.I. Rudakov and A.A. Samarsky, In Ref. 1, p. 487.

[3]G.Yonas, K.R. Prestwich, J.W. Poukey, and J.R. Freeman, Phys. Rev. Lett. 30, 164 (1973).

[4]J. Chang, M.J. Clauser, J.R.Freeman, G.R. Hadley, J.A. Halbleib, D.L. Johnson, J.G. Kelly, G.W. Kuswa, T.H. Martin, P.A. Miller, L.P. Mix, F.C. Perry, J.W. Poukey, K.R. Prestwich, S.L. Shope, D.W. Swain, A.J. Toepfer, W.H. VanDevender, M.M. Widner, T.P. Wright, and G. Yonas, Sandia Laboratories Report No. SLA 74-5176, 1974 (unpublished).

[5]F. Winterberg, Phys. Rev. 174, 212 (1968); Nucl. Fusion 12, 353 (1972).

[6]T.H. Martin, IEEE Trans. Nucl. Sci. NS-20, 289 (1973).

[7]M.W. Widner and S.L. Thompson, Sandia Report No. SAND-74-351, 1974 (unpublished).

[8]S.L. Thompson, Sandia Laboratories Report No. SAND-74-0122, 1974 (unpublished).

[9]L.M. Barker and R.E. Hollenbach, J. Appl. Phys. 43, 4669 (1972).

[10]L.M. Barker, *Behavior of Dense Media Under High Dynamic Pressure* (Gordon and Breach, New York, 1968), p. 483.

[11]J. Chang, Bull. Am. Phys. Soc. 19, 869 (1974).

[12]K.M. Gilbert, J. Chang, and L.P. Mix, Bull. Am. Phys. Soc. 19, 869 (1974).

[13]M.J. Berger and S.M. Seltzer, Oak Ridge National Laboratory, Radiation and Shielding Information Center, Computer Code Collection No. CCC-107, 1968 (unpublished).

[14]G. Yonas, American Physical Society Topical Conference, Chicago, 1974 (unpublished).

[15]J.R. Asay and L.M. Barker, J. Appl. Phys. 45, 2540 (1974).

[16]W.E. Deal, Jr., in *Modern Very High Pressure Techniques* (Butterworths, Washington, D.C., 1962), p. 200.

[17]R. Courant and K.O. Friedricks, *Supersonic Flow and Shock-waves* (Interscience, New York, 1948), p. 156.

DISTRIBUTION:
TID-4500-R66 UC-21 (208)

US Department of Energy
Washington, DC 20545
Attn: C. M. Stickley
Division of Laser Fusion

University of California
Lawrence Livermore Laboratory
P.O. Box 808
Livermore, CA 94550
Attn: M. M. May

1	M. Sparks
	Attn: W. J. Howard, 2
400	C. Wintor
1000	G. A. Fowler
1100	C. D. Broyles
1116	J. D. Plimpton
1250	R. G. Clem
1251	R. L. Hagengruber
2000	E. D. Reed
4000	A. Narath
4200	G. Yonas
4210	J. B. Gerardo
4230	M. Cowan
4241	M. J. Clauser
4242	A. J. Toepfer (10)
4253	K. R. Prestwich
4300	R. L. Peurifoy, Jr.
5000	J. K. Galt
5100	F. L. Vook
5600	D. B. Shuster
5800	R. S. Claassen
8000	T. B. Cook, Jr.
8100	W. J. Spencer
8300	B. F. Murphey
8266	E. A. Aas
3141	T. L. Werner (5)
3151	W. L. Garner (3)

For DOE/TIC (Unlimited Release)

Org.	Bldg.	Name	Rec'd by *	Org.	Bldg.	Name	Rec'd by

* Recipient must initial on classified documents.